Project Title:	Advanced Precursor Reaction Processing for $Cu(InGa)(SeS)_2$ Solar Cells
Project Period:	09/01/2011 – 05/30/2015
Project Budget:	DOE Share: $1,200,000
Submission Date:	October 12, 2015
Recipient:	University of Delaware
Address:	210 Hullihen Hall Newark, DE 19716-4602
Award Number:	DE-EE0005407
Project Team:	University of Delaware University of Florida
Principal Investigator:	William N. Shafarman Sr. Scientist Phone: 302-831-6215 Fax: 302-831-6226 Email: wns@udel.edu

Executive Summary

A number of U.S. and international companies are pursuing commercialization of Cu(InGa)$(SeS)_2$ thin film PV using absorber growth based on low cost precursor deposition followed by a high temperature chalcogen reaction step (sometimes called selenization). A primary advantage of this precursor reaction approach is the ability to utilize commercially compatible methods for the metal precursor deposition. The precursors may be reacted in a batch process with the hydride gases H_2Se and H_2S or in an in-line process in a Se or S-containing atmosphere.

This project "Advanced Precursor Reaction Processing for Cu(InGa)$(SeS)_2$ Solar Cells" was completed by the Institute of Energy Conversion (IEC) at the University of Delaware in collaboration with the Department of Chemical Engineering at the University of Florida. It developed the fundamental understanding and technology to increase module efficiency and improve the manufacturability of Cu(InGa)$(SeS)_2$ (CIGSS) films using the precursor reaction approach. A reaction process was developed that enables control of the film composition and back contact formation. The Mo/CIGSS interface was characterized and methods developed to improve adhesion and device characteristics, thereby increasing yield and module efficiency. For this purpose, the effects of interlayers between the Mo and precursor on the interface were studied. Also, the addition of Ag to the Cu-In-Ga precursor and its effect on the (AgCu)(InGa)$(SeS)_2$ (ACIGS) film reaction was investigated. The project developed a precursor structure containing Se and a reaction process to reduce processing time to five minutes and eliminate H_2Se usage, thereby increasing throughput and reducing costs.

Initially, a three-step precursor reaction process, with reaction in H_2Se at 400 – 450°C followed by an inert anneal and then reaction in H_2S at 550°C, was established using sputtered Cu-Ga-In precursors. This process was shown to prevent Ga accumulation at the back interface, leading to a more homogeneous Ga distribution, give large grain size, and form devices with open circuit voltages greater than 600 mV, efficiencies greater than 14 %, and good adhesion. The formation of voids at the back interface, commonly seen in reacted CIGSS films, was not prevented with his 3-step process. The effect of the H_2S reaction for the final reaction step was quantified. S is critical to control the surface composition and avoid Ga depletion in the CIGS which limits V_{OC} in devices.

To improve the quality of the Mo/Cu(InGa)$(SeS)_2$ interface, a study to investigate oxygen incorporation into a Mo surface layer to form MoO_3 was performed. MoO_3 was found to produce no significant changes in the properties of the reacted Cu(InGa)Se_2 film or rate of formation for its growth, but did reduce the formation of $MoSe_2$. In a second study of the Mo/CIGSS back interface, 10 nm thick Bi, Sb, or Te layers were added between the Mo and the precursor before the reaction. While no improvements in device efficiency were obtained, the addition of Te was shown to greatly reduce the formation of voids at the Mo/Cu(InGa)$(SeS)_2$ back interface and the addition of Sb improved the adhesion.

Ag-alloying was shown to have several potential benefits on the precursor structure and on the properties of reacted films. The addition of a 10 – 30 nm thick layer of Ag below the Cu-Ga-In precursors gave a much more homogeneous precursor morphology due to reduced agglomeration caused by elemental In. Reacted ACIGS films had significantly improved adhesion which enables a broader processing window including single stage reaction at temperatures above 450°C. But the change in precursor morphology with Ag did not affect the void formation at the absorber interface with Mo. A novel Ag-Ga sputter target was used to characterize different structures for Ag-Cu-Ga-In precursors and a Cu-Ga/In/Ga/Ag-Ga structure was down-selected for reaction studies. Thermodynamic assessment showed that adding Ag to the baseline Cu-Ga-In precursor provides a practical route to enhance elemental inter-mixing (via faster atomic diffusion in the liquid) and improve wetting of the substrate.

In the effort to reduce the reactive annealing time while avoiding H_2Se, Cu-In-Ga precursors were capped with elemental Se layers. This structure with a rapid thermal anneal process was used to reduce the reactive annealing time down to 5 min to form single phase CIGS or ACIGS. This approach also shows a positive effect on the film adhesion and the void formation at the back interface was largely eliminated.

Table of Contents

I. Background

A number of U.S. and international companies are pursuing commercialization of Cu(InGa)$(SeS)_2$ thin film PV using absorber growth based on low cost precursor deposition followed by a high temperature chalcogen reaction step (sometimes called selenization). A primary advantage of this precursor reaction approach is the ability to utilize manufacturing compatible techniques for the metal precursor deposition. The precursors may be reacted in a batch process with the hydride gases H_2Se and H_2S or in an in-line process in a Se or S-containing atmosphere.

Precursor reaction (often referred to as SAS for sulfization after selenization) is typically a two-step process [1]. DC sputtering is commonly selected for the precursor deposition because it is scalable using commercially available deposition equipment. It can provide good uniformity over large areas with high deposition rates, though materials utilization can be a concern. Typically, the Cu-Ga-In precursor film is sputtered from Cu-Ga and In targets where the former alleviates the problem of the Ga target melting at just above room temperature. Precursor deposition by electrodeposition or application of particles in an ink or spray have also been considered.

Reaction of the precursor films in H_2Se and H_2S can take several hours when controlled heat-up and cool-down times are included [2]. As a result, this is done as a batch process in which a large number of sample plates are processed in parallel and each process step can be independently optimized. Reaction is done in one or more large furnaces which are custom designed to withstand corrosive properties of the hydride gases while providing uniform temperature and delivery of the reactive species. An alternative process adds a Se layer to the precursor film and then reaction can be done in a relatively short process with plates continuously passed through a hot reaction zone [3]. In practice it has been found that the reaction requires additional S.

Despite the successful commercial development of the precursor reaction process, several critical issues have been identified. This includes poor adhesion at the back interface between Mo and CIGS which limits the reaction temperature during processing. The back interface also typically contains relatively large (0.1-1 μm) voids that may affect device performance or stability. A second issue is control of the through-film composition, with Ga accumulation at the back of the reacted film resulting in low bandgap near the front and consequently low voltage devices. Approaches to improve efficiency by controlling through-film composition to engineer bandgap gradients will require controlling the reaction pathways that occur during the processing from metal precursors to completed chalcopyrite absorber layer. A third issue is that the reaction process typically takes many hours when heat-up, multi-step reactions, and cool-down times are included. As a result the reaction is done as a batch process in commercial manufacturing. Significant reductions in these times can enable a continuous reaction process that should be less expensive for a large volume manufacturing plant.

The underlying technology to fabricate CIGS-based PV using the precursor reaction process is in commercial production by one company (Solar Frontier in Japan) and pilot development by others. At the start of this project, the best (unconfirmed) small area cell

result using CIGS formation by reaction of Cu-Ga-In precursors had efficiency 16.5% with V_{OC} = 0.67 V, J_{SC} = 35.0 mA/cm^2, and FF = 69.7% [4] This lagged behind the best cells using co-evaporated Cu(InGa)Se_2 primarily in the FF which in the latter case can be as high as 80%. Solar Frontier was focused specifically on FF in achieving their record performance on ~800 cm^2 modules with efficiency 16.0 %, V_{OC}/cell = 0.67V, J_{SC} = 33.7 mA/cm^2 and FF = 71%.

With this process modules with areas greater than 1 m^2 and efficiencies around 16% have been demonstrated by several companies while the highest efficiency small area laboratory cell is 20.9% [5] with open circuit voltage nearly 700 mV.

II. Introduction

This project "Advanced Precursor Reaction Processing for Cu(InGa)$(SeS)_2$ Solar Cells" completed by the Institute of Energy Conversion (IEC) at the University of Delaware in collaboration with the Department of Chemical Engineering at the University of Florida developed the fundamental understanding and technology to increase module efficiency and improve the manufacturability of Cu(InGa)$(SeS)_2$ (CIGSS) films using the precursor reaction approach currently being developed by a number of companies. Overall project objectives were to:

- Improve the quality of the Mo/CIGSS interface to improve adhesion and device characteristics, thereby increasing yield and module efficiency, respectively.
- Develop an improved precursor structure to reduce processing time to 5 minutes and eliminate H_2Se usage, thereby increasing throughput and reducing costs.

The project was performed in two Tasks with two phases of the research. Anticipated outcomes of these tasks were:

Phase 1 - Task #1: Mo/CIGSS Interface

1. A process for controlled incorporation of oxygen into the Mo surface.
2. Reaction chemistry and kinetics of Se with Mo:O_2 compared to standard Mo.
3. Cu-Ga-In precursor structures fabricated on Mo/interlayer substrates.

Phase 1 - Task #2: Precursor Structure and Reaction

1. Description of the effects of reaction conditions in the H_2Se/H_2S process.
2. Single phase CIGSS formed by reaction of Cu-Ga-In-Se precursor in H_2S.
3. A reactor built to enable H2S reaction with well-defined short reaction times.

Phase 2 - Task #1: Mo/CIGSS Interface

1. Application of interlayers between the Mo and Cu-Ga-In precursor to suppress on void formation and control $MoSe_2$.
2. Reaction pathway and kinetics of Se with Mo/interlayer structures.
3. ACIGS films formed and the effect of Ag on the back interface determined.
4. A description of the effect of Na incorporation on the formation of voids, $MoSe_2$ and adhesion.

Phase 2 - Task #2: Precursor Structure and Reaction

1. Quantitative description of the effects of reaction conditions in the H_2Se/H_2S process.
2. A process for formation of single phase CIGSS by 5 min H_2S reaction.
3. Description of the effect of Ag addition on reaction pathways to form ACIGSS.
4. Quantitative analysis of the effect of voids on CIGSS solar cells.

The project had one Phase 1 Go/No-Go milestone to demonstrate a solar cell using a precursor-reacted Cu(InGa)$(SeS)_2$ absorber with efficiency ≥ 14% and FF ≥ 74%. This milestone was met using the optimized baseline process and modified processes including the use of Ag to allow a higher temperature, faster process. Two final milestones were:

1. Demonstrate a solar cell using a precursor reacted Cu(InGa)$(SeS)_2$ absorber with efficiency ≥ 18% and FF ≥ 76%.
2. Demonstrate a solar cell using a precursor reacted Cu(InGa)$(SeS)_2$ absorber with efficiency ≥16% and FF ≥ 76% using reaction time ≤ 5 minutes and no H_2Se.

These milestones were not achieved. The project focused primarily on understanding the fundamentals of the precursor formation and reaction process. Less effort than anticipated was placed on device performance, and no effort was given to implementation of anti-reflection layers and optimized buffer layers that would improve device efficiency. Instead the main effort was place on addressing the list of project objectives stated above.

III. Project Results and Discussion

Results are described below in three sections. First the baseline process developed in this project is described. This includes the sputtered Cu-Ga-In precursor and the three-stage $H_2Se/Ar/H_2S$ reaction process. Control of the film composition through the development and understanding of the reaction process was a key focus of the project. These processes for the basis for experiments to characterize the Mo/Cu(InGa)$(SeS)_2$ interface described in Task #1 and to modify the process through control of the surface, the incorporation of Ag and using a Se-capped precursor to enable a faster reaction without H_2Se.

Process Description and Characterization

Cu-Ga-In Precursor

The precursor structure used as the basis for this project was a sputtered Cu-Ga-In precursor deposited onto a 2.5 cm x 2.5 cm soda lime glass substrate sputter-coated with a 700 nm thick sputtered Mo back contact. Precursors were sputter deposited from In and $Cu_{0.77}Ga_{0.23}$ targets. The sputtering system was configured with a platen rotating 5 rpm so that 350 alternating layers of In and $Cu_{0.8}Ga_{0.2}$ were deposited corresponding to 700 nm. This is targeted to form a fully reacted CIGSS film with 1.8 µm thickness.

SEM images of an as-sputtered precursor in Figure 1 show nodules distributed on a smooth background. Although the metal precursor was prepared by repetition of many In and Cu-Ga layers, significant agglomeration occured and a smooth layered structure was not obtained. Table 1 shows wide-area and spot-EDS measurements taken from Figure 1. The wide area average EDS measurements give composition ratios Cu/(In+Ga) = 0.82 and Ga/ (In+Ga) = 0.19. Spot-EDS measurements of the “nodules” and the smooth “background” show significant differences in composition. The nodules are In-rich, while the smooth background is Cu-rich and Ga-rich compared to the average composition.

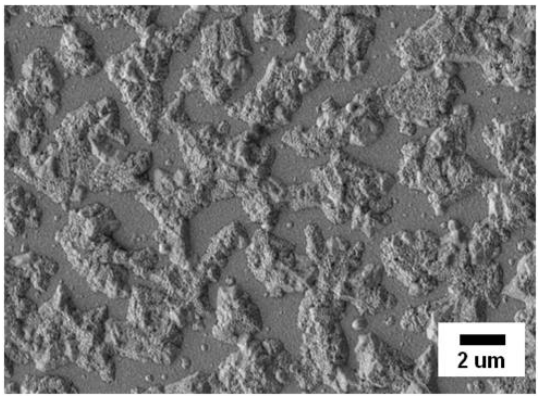

Figure 1. Plan-view SEM images of a Cu-In-Ga metal precursor.

XRD spectra taken with incident beam angles of 0.5º and 4º are shown in Figure 2. Since both Cu and Ga solubility in In are low, almost pure In and intermetallics such as Cu_3Ga, Cu_4In, and $Cu_9(In_{1-x}Ga_x)_4$ are observed [6,7]. The value of x in the $Cu_9(In_{1-x}Ga_x)_4$ phase is determined to be ~0.4 by applying Vegard's law. Comparison of the different incident angles shows that the surface is relatively In-rich and the bulk film

contains the Cu-rich intermetallic phases. Therefore wide-area EDS measurements lead to overestimation of the relative In composition. Even though the measured average Cu/(In+Ga) ratio of the metal precursor is 0.82, the reacted film is expected to yield higher Cu/(In+Ga).

Table 1. Compositional values of wide-area and spot-EDS measurements taken from Figure 1.

EDS measurement location	Cu (at%)	In (at%)	Ga (at%)	Mo (at%)	Cu/(In+Ga)	Ga/(In+Ga)
Average	38.4	37.9	8.7	15.1	0.82	0.19
Nodule	35.6	43.6	8.1	12.6	0.69	0.16
Background	41.2	25.2	9.7	23.0	1.18	0.28

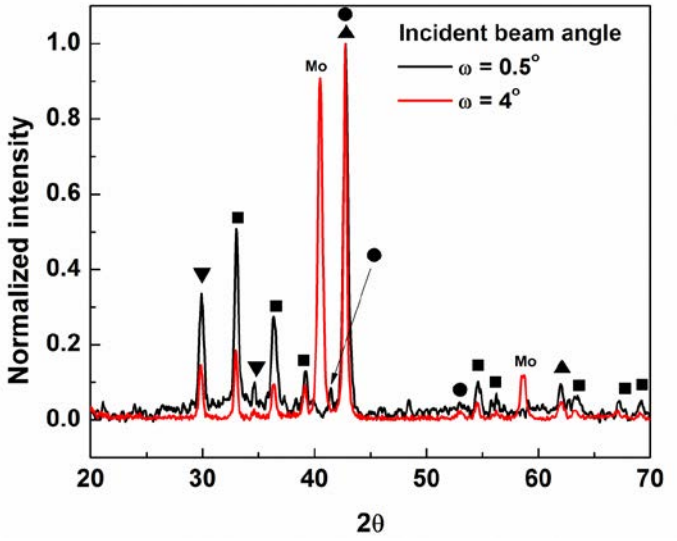

Figure 2. Asymmetric XRD spectra of a Cu-In-Ga metal precursor. XRD patterns were taken from incident angles of 0.5º (black) and 4º (red). Symbols of ■, ●, ▲, and ▼indicate In, Cu_3Ga, Cu_4In, $Cu_9(In_{1-x},Ga_x)_4$, respectively.

Three-step $H_2Se/Ar/H_2S$ Reaction

A 3-step $H_2Se/Ar/H_2S$ reaction of sputtered Cu-Ga-In precursors was developed at IEC and characterized under this project [8]. This 3-step reaction forms $Cu(InGa)(SeS)_2$ films with large grain size, controlled Ga distribution through the film, and good adhesion. Nevertheless, the $Cu(InGa)(SeS)_2$ films still include voids at the Mo/$Cu(InGa)(SeS)_2$ interface which may be caused by the agglomeration of a slow-reacting Cu_9Ga_4 intermetallic phase at the back of the film or by film expansion.

Sputtered metal precursors throughout this project were reacted in IEC's 2" diameter quartz tube reactor shown in Figure 3. Safety features include hydride gas detectors interlocked into building alarms and automated shut-down capabilities, pressure monitors similarly interlocked into automated shut-down capabilities, a two-stage gas

scrubber, check-off procedures for handling and changing gas cylinders, and a back-up generator to ensure continuous operation of detectors and ventilation.

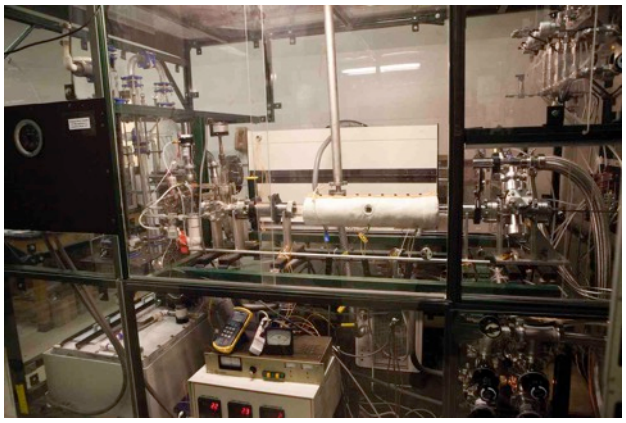

Figure 3. IEC H_2Se/H_2S reactor including 2" and 6" quartz reactor tubes and gas scrubber at left.

The three-step reaction sequence is schematically shown in Figure 4. Before reaction, the reactor was evacuated to 5 $x10^{-6}$ Torr to remove moisture and impurities. Then, a $H_2Se(0.35\%)/O_2(0.0035\%)/Ar$(balance) mixture was introduced and selenization was performed (1^{st} step) at 400ºC for 50 min. After the H_2Se and O_2 flows were stopped, a 10 min dwell at 400ºC prevented uncontrollable/nonuniform reaction due to residual reactive gases during ramp-up to higher temperature. Then, the temperature was ramped up to 550 ºC and the samples annealed for 20 min under Ar atmosphere (2^{nd} step). Finally, sulfization at 550 ºC for 10 min was performed with $H_2S(0.35\%)/O_2(0.0035\%)/Ar$(balance) ($3^{rd}$ step). After sulfization, samples were pulled from the hot reaction zone of the tube to prevent further reaction. The addition of O_2 into the reactions is to prevent agglomeration by forming a thin oxide layer on the top surface and to enhance the dissociation rate of the hydride gases [8,9].

A detailed characterization of the three-step reaction process and film evolution has been completed [8,10]. Figure 5 shows cross-sectional SEM images of films after each reaction step and Figure 6 shows Ga/(Ga+In) and S/(Se+S) composition ratios through the film depth. First, the Cu-Ga-In metal precursors are selenized at 400ºC for 50 min. The films are partly converted to chalcopyrite with fine microstructure and a slow reacting Cu-Ga intermetallic remaining at the Mo surface. The Ga/(Ga+In) ratio increases near the Mo back contact where a Cu_9Ga_4 intermetallic phase can be observed by XRD when the film is peeled away from the Mo contact. With the 2^{nd}-step Ar anneal at 550ºC for 20 min, significant recrystallization (Figure 5) and Ga homogenization (Figure 6) occur. However an InSe phase develops from the CIGS/Mo interface due to insufficient Se which leads to decomposition of the CIS. The 3^{rd}-step sulfization results in S incorporation near the surface and completely removes the InSe phase while maintaining the Ga/(Ga+In) profile and large grains.

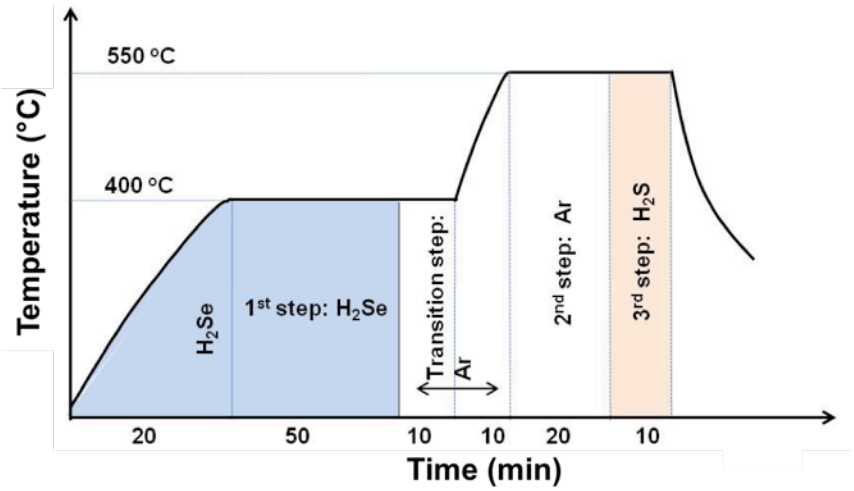

Figure 4. Temperature-time schematic of the 3-step $H_2Se/Ar/H_2S$ reaction process.

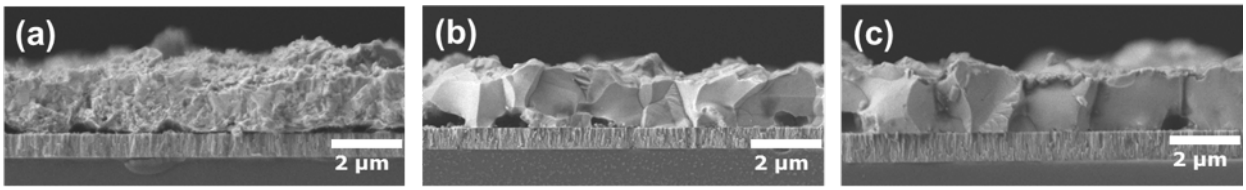

Figure 5. Cross-sectional SEM images after each step: (a) 1st-step selenization, (b) 2nd-step Ar anneal and (c) 3rd-step sulfization.

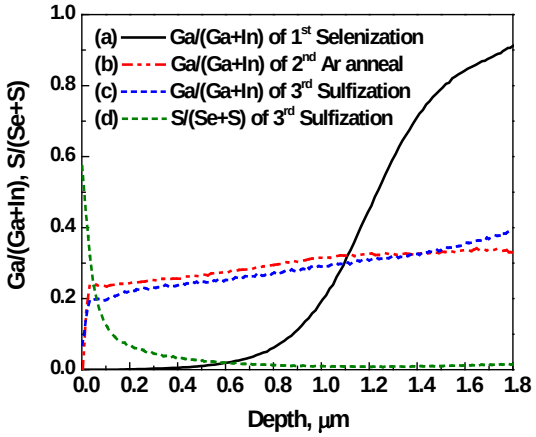

Figure 6. Depth-dependent Ga/(Ga+In) and S/(Se+S) ratios after each step.

A series of reactions were done to further elucidate the grain growth and Ga-redistribution during the Ar annealing step, before S is added to the film. Reactions were stopped at a series of intermediate points as indicated in Figure 7(a) [10]. XRD scans shown in Figure 7(b) show the evolution of the film by focusing on the (112) peak at ~27º. At points "1" and "2" the CIGS film does not exhibit any significant difference from the CIGS film after the 1st step with little negligible Ga incorporation. At point 3 the film exhibits a slight (112) peak shift to higher Ga content while also developing an additional peak around 27º. The film then undergoes an abrupt change between points

"3" and "4" from 495 to 530ºC. InSe develops such that its (004) peak intensity exceeds that of CIGS (112). In addition, the CIGS (112) peak shifts to 26.88º, indicating Ga incorporation, and its intensity increases. The rest of the 2nd-step exhibits a small increase of (112) peak intensity suggesting that recrystallization and grain growth. The peak intensity of InSe also decreases after point "4" for reasons not currently understood but it isn't eliminated until S is added in the 3rd step.

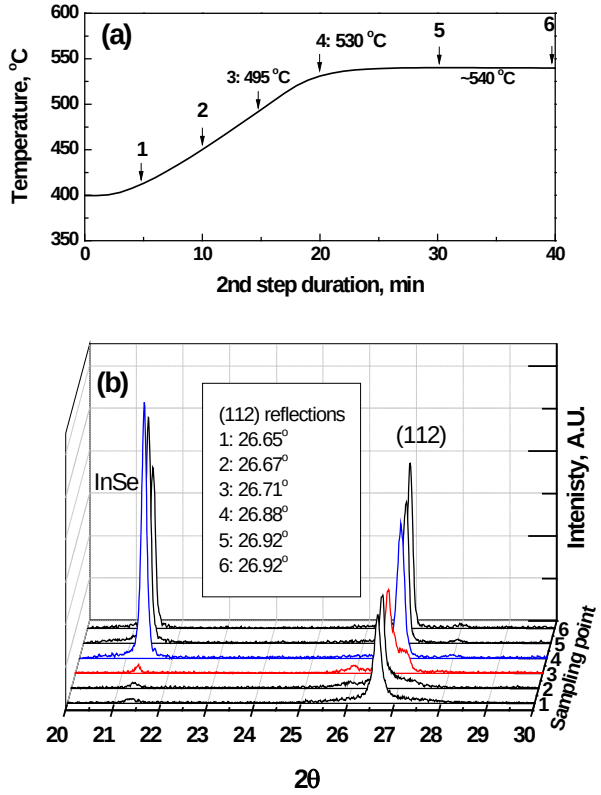

Figure 7 Temperature profile of the tube reactor during the 2nd step. Numbers indicate the points where samples were pulled out from the reactor (a). XRD patterns corresponding to each sample point (b).

A possible explanation for the abrupt recrystallization and Ga homogenization at T = 495ºC could be due to the Cu_9Ga_4 intermetallic which can be present as a mixture of liquid Ga and solid γ1 phase (Cu_9Ga_4) above 485ºC [11]. Thus, the liquid Ga phase might rapidly diffuse through CIGS grain boundaries. For comparison, a $CuInSe_2$ (CIS) film formed by the 3-step reaction using a CuIn precursor exhibits smaller grains than the CIGSS film as shown in Figure 5 since there is no Cu_9Ga_4 intermetallic formation at the film's back.

Two key advantages of the 3-step reaction process have been described in refs. 6, 8, and 10. First is the control of relative Ga profile through the film achieved by redistribution of the Ga as temperature is increased. This occurs only if there is sufficient Cu_9Ga_4 phase after the 1st-step because the time and temperature are restricted so CIGS reaction is incomplete. The second advantage is minimal formation of $MoSe_2$ at the back contact. Since the critical recrystallization of the film occurs in an

Ar atmosphere with insufficient Se+S to complete the reaction, no excess Se is available at the back. A small $MoSe_2$ peak can be observed by glancing incidence XRD on the Mo only after the 3rd-step [8].

High temperature XRD (HTXRD) studies as described in ref. 12 have been used throughout this project to provide a detailed understand of reactions to form CIGS-alloys. A temperature ramp selenization of a baseline Cu-Ga-In precursor in elemental Se is shown in Figure 8. In this reaction, In-rich CIGS formed at ~290°C simultaneous with the decomposition of the γ-$Cu_9(Ga_xIn_{1-x})_4$ phase. CuSe and In_4Se_3 also formed at this temperature, likely from Cu and In of the γ phase not forming CIGS. Two separate CIGS phases were present as CuSe decomposes to $Cu_{2-x}Se$ + Se-rich liquid at 310°C. The $Cu_{2-x}Se$ solid solution formed at 310°C simultaneously during CuSe monotectic decomposition to yield a Se-rich liquid (not evident in XRD pattern). $CuGaSe_2$ formed as was indicated by a separate (112) chalcopyrite peak. Formation of $CuGaSe_2$ indicated that some Ga may not have reacted after the decomposition of the γ phase. These HTXRD results appear to contradict the observation of $Cu_9(Ga_xIn_{1-x})_4$ that persists at the back of reacted films even after 550ºC reaction [6,8]. However, the presence of this phase at the back of the film could only be observed after separating CIGS films from the Mo back contact to directly access the residual phases adherent to the Mo.

Figure 8 also shows that Ga-In alloying in CIGS increased with temperature but complete homogenization was not fully reached. In-rich CIGS and $CuGaSe_2$ slowly mixed as the temperature was increased but even at 600°C, two separate compositions were evident.

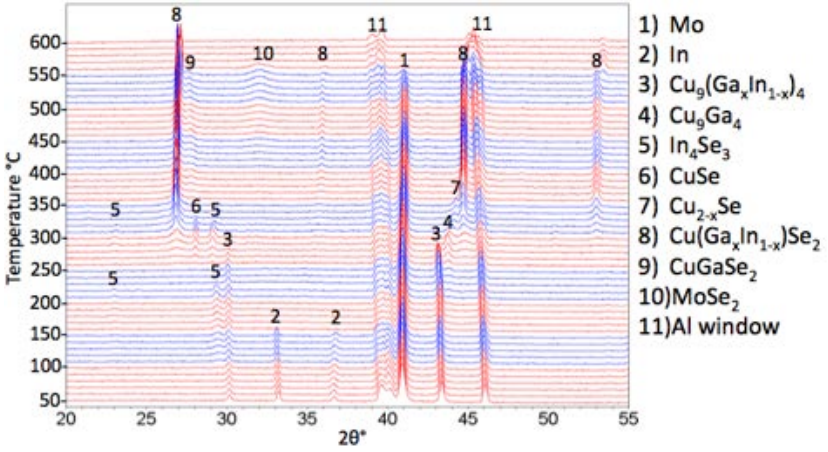

Figure 8. Temperature ramp selenization of SLG/Mo/Cu-In-Ga.

All devices reported in this report were fabricated with a Mo/CIGSS/CdS/i-ZnO/ITO/Ni-Al structure. A 50 nm thick CdS layer was deposited on the CIGSS absorber layer by chemical bath deposition (CBD) and i-ZnO (50 nm)/ITO (150 nm) layers with sheet resistance 30 Ω/sq were deposited by RF magnetron sputtering. Finally, grid of Ni (50 nm)/Al (3000 nm) was deposited by e-beam evaporation. Cells were delineated by mechanical scribing with areas 0.4 or 1.0 cm^2. No devices had an additional anti-

reflection layer though an evaporated MgF_2 layer could be used to increase J_{SC} and improve efficiencies by 1- 1.5 % absolute.

The baseline process as described produces solar cell devices with 14-15% efficiency as shown in Figure 9. Typical J-V parameters are V_{OC} = 600 - 620 mV, J_{SC} = 32 mA/cm^2, FF = 72-74%. QE shows a long wavelength edge indicating a bandgap 1.1 – 1.15 eV, consistent with incorporation of [Ga]/[In+Ga] = 15 - 20% at the front of the absorber layer.

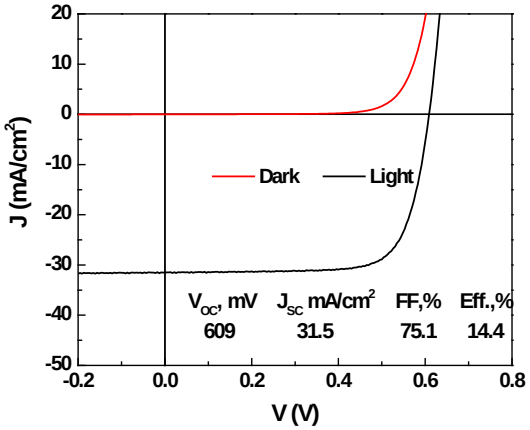

Figure 9. JV characteristics of Cu(InGa)$(SeS)_2$ cell with three-step reaction.

Task #1: Mo / Cu(InGa)$(SeS)_2$ Interface

The overall objective of this task was to develop processes for modifying the Mo surface or the interface between the Mo and Cu-Ga-In precursor to control void formation and adhesion issues. Two approaches have been investigated: 1) the insertion of an interlayer between the Mo and Cu-In-Ga metal precursor to modify the surface energy and potentially prevent the agglomeration of Cu-Ga intermetallic; and 2) formation of an oxide layer on the Mo surface.

Ag Interlayer

Ag alloying was investigated as an interlayer between the Mo and the Cu-Ga-In precursor because it lowers the melting temperature of CIGS [13] so increased atomic mobility during film reaction may enhance intermixing of Ga and affect void formation. To characterize the effect of the Ag addition to the precursor, a Cu-In-Ga and three types of Ag-Cu-In-Ga precursors were prepared by dc magnetron sputtering from $Cu_{0.77}Ga_{0.23}$, In and Ag targets onto Mo/soda-lime glass substrates at room temperature [14]. All precursors had Ga/(In+Ga) ≈ 0.2 and their total thicknesses were adjusted to give 1.8 µm thick CIGS and ACIGS after selenization. Sample A was the baseline precursor described on page 9. Sample B included a 32 nm thick Ag layer on the Mo followed by a baseline Cu-Ga-In layer. Sample C had a 5 nm thick Ag layer on the Mo, again followed by a similar Cu-Ga-In layer. Sample D was a 230 nm thick $Cu_{0.77}Ga_{0.23}$ layer followed by a 460 nm co-sputtered Ag + In layer.

Figure 10 shows SEM micrographs of the precursors. The Cu-In-Ga precursor A had large In-rich nodules on a smooth Cu-Ga background as in Figure 1. Precursor B with a 32 nm thick Ag layer under the Cu-Ga-In showed a fine grained surface compared with the control Cu-In-Ga precursor and much less agglomeration. EDS results [14] indicated that the Ag does not stay at the back of the film but is distributed indicating that it diffused into Cu-Ga-In during the sputtering process. In spite of the very thin 5 nm Ag layer, precursor C also showed a fine grained surface. Precursor D has nodules on a background layer of small grains. Unlike the Ag-free precursor A, the nodules in this case consist of In and Ag in a 5:1 ratio. The background layer (darker regions in Figure 10(d)) consists of 39% Cu, 36% In, 14% Ag and 11% Ga. Again, the Ag was distributed throughout the film.

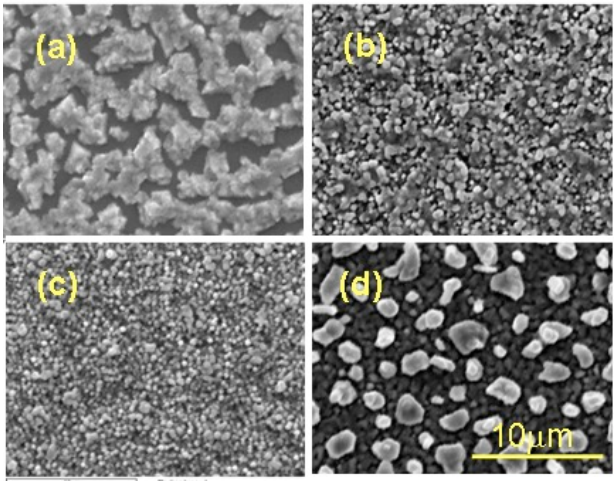

Figure 10. SEM micrographs of metal precursors. (a) Sample A. (b) Sample B .(c) Sample C. and (d) Sample D.

Figure 11 shows XRD patterns of the four precursors. Precursor A consists of In, Cu_4In, and $Cu_9(In,Ga)_4$ phases. The Ag layers in precursors B and C lead to a different structure with only the intermetallic compounds, CuIn, $AgIn_2$, and $Cu_9(In,Ga)_4$ present. The peaks identified as $AgIn_2$ are all at slightly lower 2-θ than in the powder diffraction pattern [15], so it is presumed that Ga, with larger atomic radius substitutes part of the In and forms $Ag(In,Ga)_2$. The dramatic difference in morphology between the Cu-Ga-In and Ag/Cu-Ga-In precursors can be attributed to the absence of the elemental In phase which, due to its low melting temperature leads to nodule agglomeration. Finally, precursor D contains In, $Ag(In,Ga)_2$ and $Cu_4(In,Ga)$. EDS results suggest that the larger nodules contain mostly In so the small nodules are $Ag(In,Ga)_2$ and $Cu_4(In,Ga)$.

Precursors A-D were reacted at atmospheric pressure in 0.35%H_2Se / 0.0035% O_2 /Ar using a single step reaction at 475ºC for 90 min. After reaction, Ag and Cu were uniformly distributed through the film although Ga remained near the back of the film as with Cu-Ga-In precursors. While the surface morphology of the precursors is very different, there is less difference in the surfaces of the selenized films [14].

Samples with 5 and 32 nm Ag interlayers were further characterized by an HTXRD study during their selenization in elemental Se. Results shown in Figure 12 can be

compared to those in Figure 8 above for the selenization of the baseline precursor. The result again show that the addition of Ag eliminated In in the precursor by forming $AgIn_2$ and thus changed the reaction pathway. Chalcopyrite can by observed as early as 280°C when Ag was in the precursor.

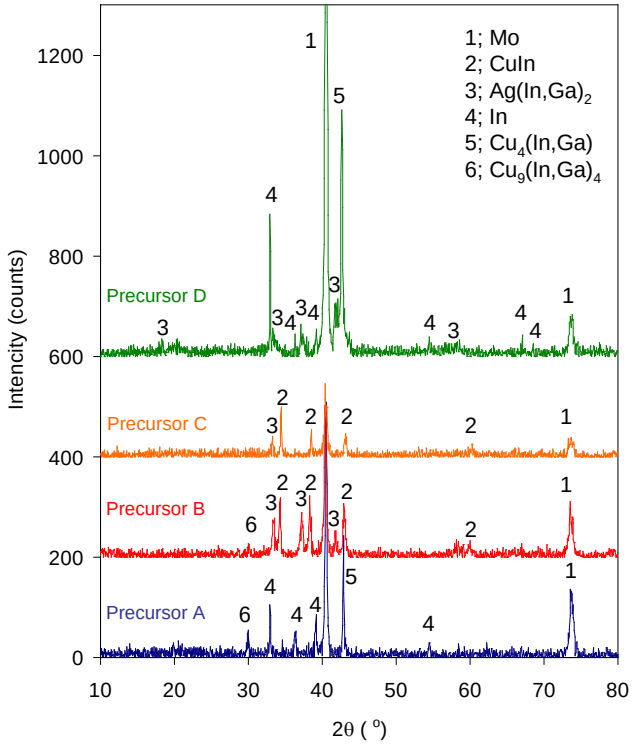

Figure 11. XRD spectra of precursors A-D with observed phases identified.

All samples have voids at the backside observed after lifting off from the Mo surface but the voids in samples B and C are smaller than the others. XRD spectra after selenization showed a single chalcopyrite phase on each sample with the Ag incorporated to form (AgCu)(InGa)Se_2 (ACIGS). Finally, devices were fabricated from the selenized films but the CIGS on sample A peeled off from the Mo back contact during the CdS deposition. Samples B, C and D didn't show any evidence of delamination demonstrating that the Ag incorporation improved adhesion at the ACIGS/Mo interface. Thus the inclusion of Ag, even in the top layer of the precursor as in sample D, enables a simple single-step reaction process at temperatures which cannot be used for reaction of Cu-Ga-In precursors due to poor adhesion.

Significantly improved adhesion with Ag addition was also observed when samples were peeled off to expose the back contact for characterization.

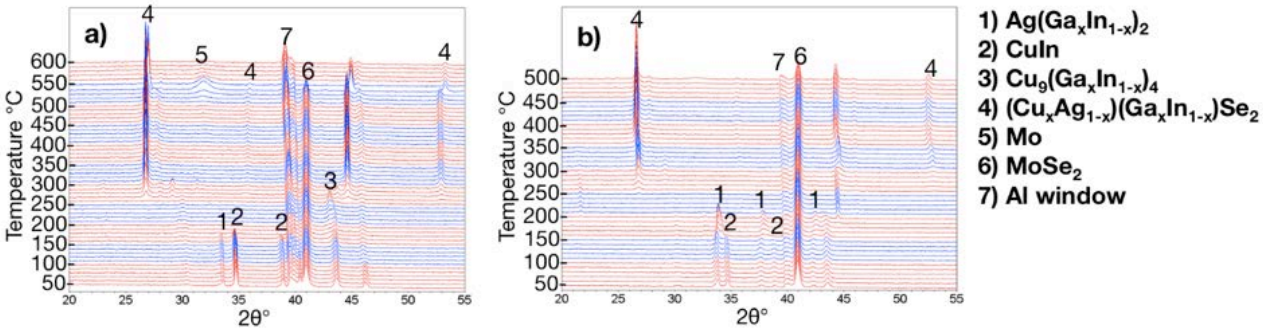

Figure 12. Temperature ramp selenization of a) SLG/Mo/Ag(5nm)/CIG(630nm) and b) SLG/Mo/Ag(32nm)/CIG(630nm)

To spatially understand the formation of the chalcopyrite phase with the addition of Ag, a sample of SLG/Mo/Ag(32nm)/Cu-In-Ga(630nm) was reacted with Se at 280°C for 5 min and then quenched to room temperature in approximately 20 s. This was

characterized by TEM paired with EDS as shown in Figure 13. TEM-EDS showed that Ga was segregated towards that Mo back-contact while a Ag-rich Ag-Cu-In-Se phase appeared to form at the upper surface during selenization.

Observation of the ACIGS peak area growth during isothermal selenization allowed estimation of ACIGS formation rates which are plotted in Figure 14. These formation rates revealed that the activation energy for chalcopyrite formation decreased with increasing Ag/(Ag+Cu) in the precursor. ACIGS growth does not follow an Avrami (nucleation and growth) or a parabolic (layer by layer) growth model at all temperatures

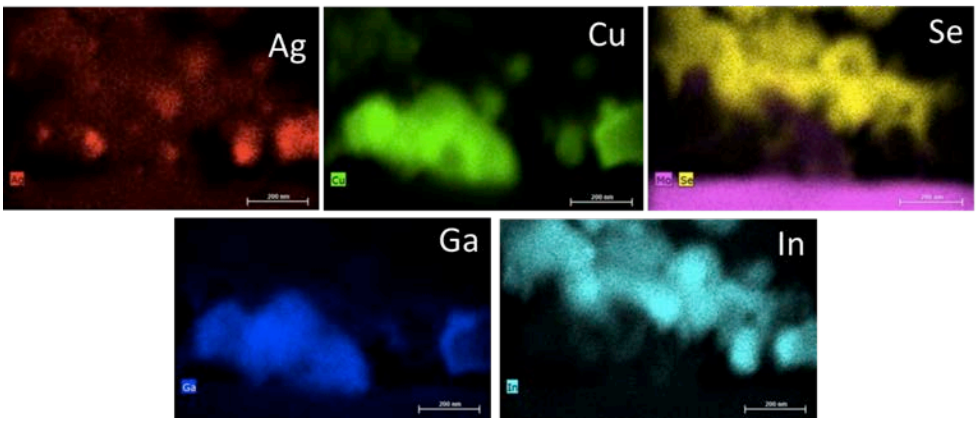

Figure 13. Room temperature TEM-EDS composition mapping of SLG/Mo/Ag(32nm)/CIG(630nm) after it had reacted with Se at 280°C for five minutes. Mo is highlighted in pink in the Se composition map to show the location of the back contact.

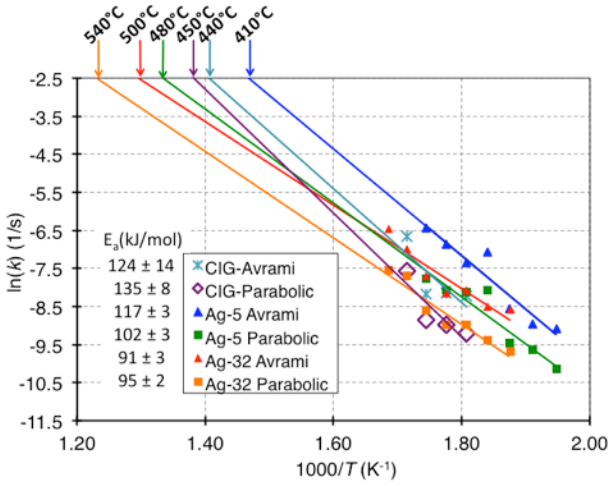

Figure 14. Arrhenius plot of chalcopyrite formation rate vs. 1/T K for SLG/Mo /CIG(700nm), SLG/Mo/Ag(5nm)/CIG(630nm), and SLG/Mo/Ag(32nm)/CIG(630nm). Estimated activation energies derived rate constants for each set of isothermal runs. Extrapolated rate to ln(k)=-2.5 indicates temperature required for 99.999% conversion of precursor film to CIGS in 2 min.

Table 2 shows device parameters and Figure 15 shows J-V curves for the best cells on samples B, C and D after the 1-step H_2Se reaction at 475ºC for 90 min. The relatively

low V_{OC} and high J_{SC} of samples B and C compared to the average Ga/(In+Ga) in the precursor are consistent with low Ga content in the active front part of the absorber as observed in EDS measurements and consistent with XRD peak positons [14].

Table 2. J-V parameters of devices using absorber layers formed by the reaction of precursors A-D at 475ºC for 90 minutes.

	V_{oc} (V)	J_{sc} (mA/cm^2)	FF (%)	Efficiency (%)
A	-	-	-	-
B	0.55	37.2	67.8	13.9
C	0.53	35.3	66.3	12.4
D	0.48	31.8	51.0	7.7

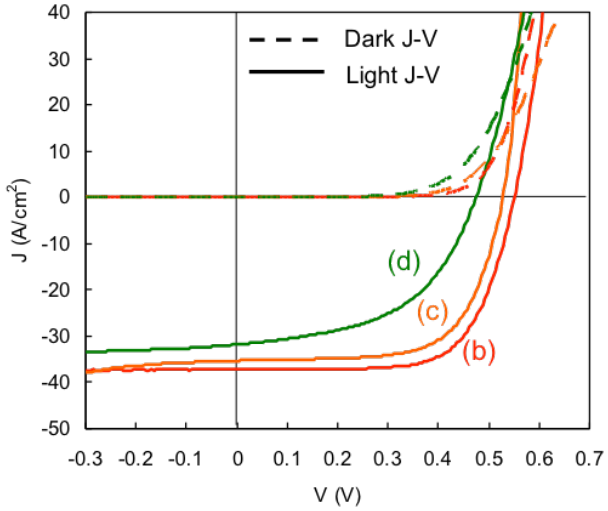

Figure 15. J-V curves for devices with absorber layers from the reaction of precursors A-D

Ag incorporation using a Ag/Cu-Ga-In precursor with a 32 nm-thick Ag layer was also characterized using a three-step reaction modified from that shown in Figure 4. The 3-step reaction in this case was H_2Se at 500ºC for 10 min followed by Ar at 550ºC for 20 min and H_2S at 550ºC for 10 min taking advantage of the improved adhesion afforded by the Ag interlayer. Figure 16 shows cross-section SEM images of CIGSS and ACIGSS films. The fine microstructure of each film was attributed to a greater extent of selenization due to the 500ºC reaction temperature for the 1st step.

The ACIGSS films were found to have more voids near the Mo back contact, again indicating that Ag layer addition does not suppress the void formation. This shows that the void formation is not correlated to the In agglomeration in the metal precursor film. The CIGSS film appeared to have a nearly void-free interface suggesting that the void formation could instead be controlled by the high selenization temperature. In spite of the void-free interface, however, the CIGSS film delaminated during the CBD-CdS deposition. In contrast, the Ag incorporation again improved the adhesion and the (AgCu)(InGa)$(SeS)_2$ solar cell gave an efficiency of 15.1% with FF = 73.1% and V_{OC} = 569 mV (Figure 16(c)). The lower V_{OC} of the ACIGSS cell was due to lower Ga content in the metal precursor since some content of Cu and Ga was replaced with Ag.

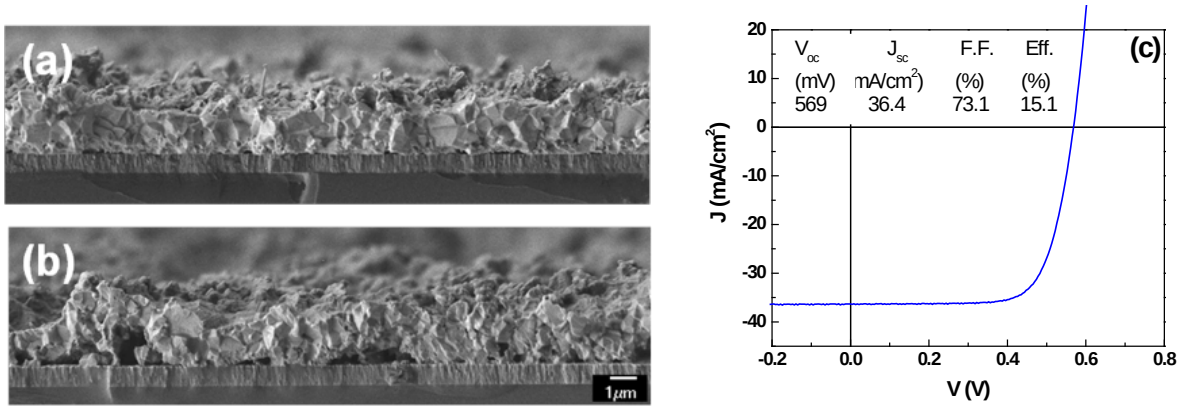

Figure 16. Cross-sectional SEM images of reacted CIGSS (a) and ACIGSS (b), and JV curve of 15.1%-efficient reacted (AgCu)(InGa)Se_2 solar cell (c).

Sb, Bi, and Te Interlayers

The group V elements, Sb and Bi, have been reported to enhance recrystallization of CIGSS via a surfactant effect [16,17]. And Te has been shown to induece wetting of metallic species on Mo [18]. In this project, the incorporation of Sb, Bi or Te interlayers before the metal precursor was investigated to promote greater intermixing/dispersing of the Cu-Ga intermetallic, induce more uniform selenization and minimize void formation by reducing the slow-reacting Cu_xGa intermetallic.

Using electron-beam evaporation, 10 nm-thick Sb, Bi, and Te thin layers were deposited onto Mo-coated soda-lime glass. Then, baseline Cu-In-Ga metal precursors were deposited. With the interlayers, precursor morphologies were modified. In particular SEM and glancing incidence XRD showed that the Te interlayer mitigated compositional/phase non-homogeneity due to In agglomeration [19]. This enhanced intermixing may reduce the agglomeration of the slow-reacting $Cu_9(Ga,In)_4$ phase which could affect void formation.

The precursors were reacted using the baseline 3-step process (Figure 4). Figure 17 shows cross-sectional SEM images of the reacted CIGSS films with and without interlayers. The Sb and Te incorporation appear to enhance recrystallization, whereas the Bi incorporation does not have any noticeable difference on grain size. All the samples had voids at the Cu(InGa)$(SeS)_2$/Mo interface but the Te interlayer reduced void density by about 30 % compared to the control. The Bi-interlayer resulted in a very porous interface as seen in Figure 17(c) and the films had poor adhesion due to delamination of the CIGSS absorber from the Mo back contact.

The adhesion of each CIGSS absorber was evaluated by a delamination test, measuring the force to peel a CIGSS absorber off from the Mo back contact using a 1/8”diameter stub glued to the film. Table 3 gives the applied forces to delaminate the CIGSS absorbers. The Sb-incorporation turned out to significantly improve the adhesion of the CIGSS film, while the Bi-incorporation gave the smallest force for delamination.

Even though the Te-incorporated CIGSS film had smaller void density and greater grain size than the control, it did not improve the adhesion of the CIGSS film.

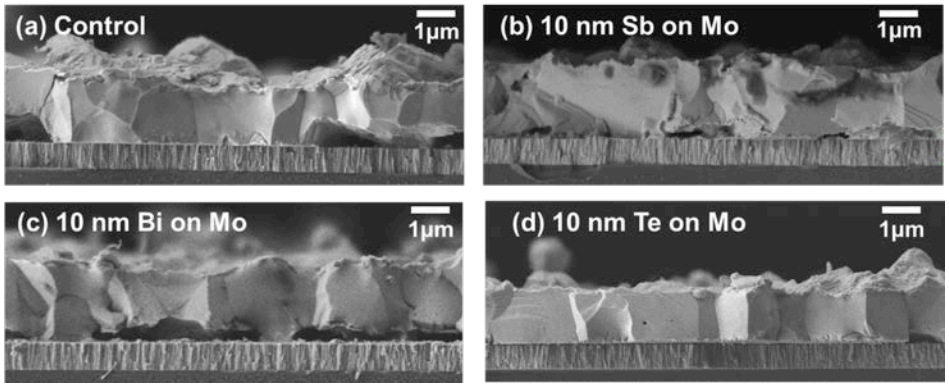

Figure 17. Cross-sectional SEM images of reacted CIGSS absorbers with or without interlayer: (a) control (no interlayer), (b) Sb interlayer, (c) Bi interlayer and (d) Te interlayer

Table 3. Adhesion measurements for each absorber. Uncertainty is determined by the standarad deviaion from 4 tests. The detection limit is ~ 1500 psi.

Interlayer	Control	Sb	Bi	Te
Applied force/ unit area, (psi)	1160 ± 180	> 1500	760 ± 200	1030 ± 200

Figure 18 shows SIMS compositional depth profiles of the CIGSS samples deposited on different interlayers. The Sb- and Te-incorporated CIGSS films exhibited a steeper Ga grading than the control film, suggesting the 1st-step selenization was enhanced by inserting the Sb- or Te-interlayer. The Sb-incorporated CIGSS absorber also exhibited a S accumulation near the Mo back contact. In contrast with the main constituents, the Na profiles were found to be more affected by the interlayers. The Te-incorporated CIGSS absorber had similar Na concentration [Na] as the control sample, while the Sb- and Bi-incorporated CIGSS absorbers had lower [Na].

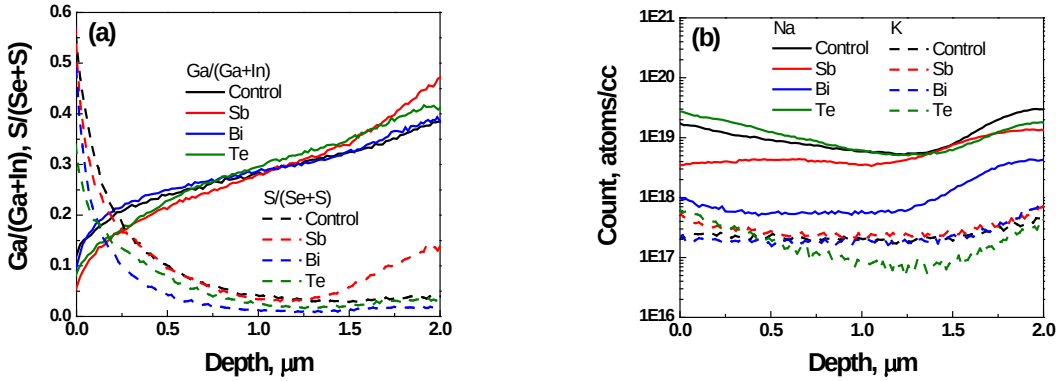

Figure 18. SIMS profiles of reacted CIGSS absorbers: (a) Ga/(Ga+In) and S/(Se+S) ratios and (b) alkali (Na and K) contents. The thicknesses of each film were normalized to the average 2 μm.

JV results of each device using the different interlayers are shown in Figure 19 and their related parameters are summarized inTable 4. The control sample had efficiency η = 13.3% with V_{OC} = 612 mV, whereas the Sb-, Bi-, and Te-incorporated cells yielded lower efficiency and V_{OC}. Sb lowered all the device parameters, whereas Te and Bi mainly degraded V_{OC}. The V_{OC} drop in the Te-incorporated cell is relatively small, 40 mV, and this may be ascribed to smaller Ga and S [19]. This can be improved with modification of the time/temperature profile to reduce the extent of the selenization reaction in the 1st step. In contrast, the Bi-incorporated cell exhibited significantly smaller V_{OC} than the Te-incorporated cell, which is presumably attributed to the lower Na content in the CIGSS absorber as shown in Figure 18(b). The poor device performance of the Sb-incorporated cell has not been clearly explained. However, the external quantum efficiency in Figure 19(b) of the Sb-incorporated cell is significantly lower in the long wavelength region than the other samples. This suggests poor bulk properties (e.g. higher defect density) leading to higher recombination and thus poorer J_{SC} and V_{OC} with the Sb-incorporation.

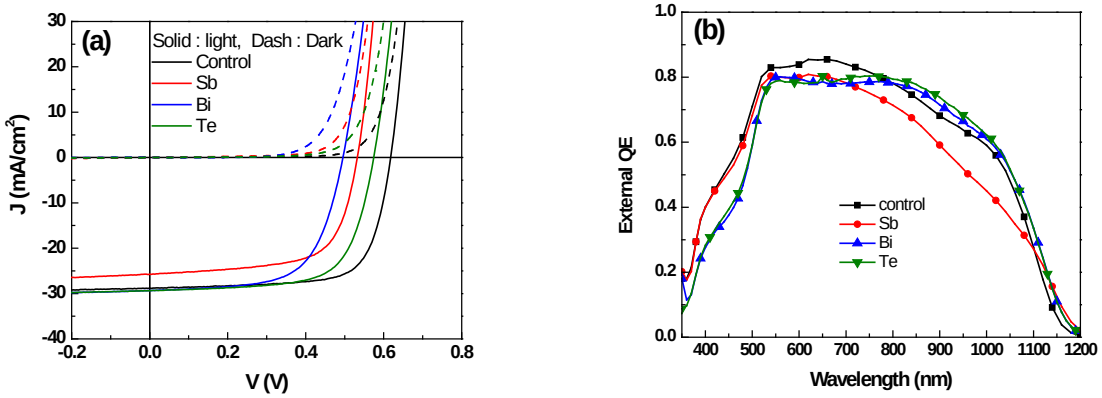

Figure 19. J-V characteristics (a) and external quantum efficiencies (b) of CIGSS cells with or without interlayer

Table 4. J-V values of the cells shown in Figure 18

Interlayer	V_{OC} (mV)	J_{SC} (mA/cm^2)	FF (%)	□□□□ (%)
Control	612	30.3	71.9	13.3
Sb	534	25.7	66.1	9.1
Bi	494	29.4	64.0	9.3
Te	574	29.5	68.5	11.6

Mo-O Back Contact

The incorporation of oxygen into the surface of the Mo contact was proposed as an approach to improve adhesion by suppressing or modifying [20] the formation of $MoSe_2$ at the Mo/CIGSS interface during selenization. Thus, a Mo/MoO_3 back contact structure was being evaluated utilizing MoO_3 deposited by reactive sputtering as developed at IEC under a different project[21,22]. MoO_3 films were 10 nm thick and were deposited with either 10% or 35% O_2/(Ar+O_2) sputtering atmosphere.

Cu(InGa)$(SeS)_2$ films with or without a MoO_3 layer were formed using IEC's baseline 3-step reaction process. No differences in surface morphology, grain size, or Cu(InGa)$(SeS)_2$ film adhesion were observed between the control and MoO_3 samples. In addition, all Cu(InGa)$(SeS)_2$ films exhibit similar void formation at the Cu(InGa)$(SeS)_2$/back contact interface. GIXRD spectra of the Mo surface after delamination are shown in Figure 20. Again, the difference among samples is not significant. $MoSe_2$ is barely detected on the Mo for the control sample and therefore the effect of the MoO_3 layers is minimal.

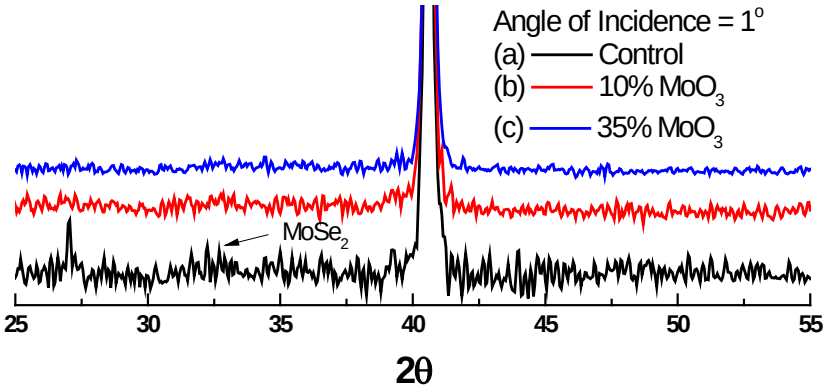

Figure 20. GIXRD patterns of Mo surface: (a) control, 10% MoO_3, and (c) 35% MoO_3

Figure 21(a) shows the Na depth profiles of each sample, suggesting the MoO_3 layer, particularly at 35% O_2, impedes Na diffusion to the CIGS bulk. Furthermore, increases in O_2 sputter pressure appear to decrease the Na content at the CIGSS front surface. Note that the depth profiles of Ga/(In+Ga) and S/(Se+S) were not affected by the presence of the MoO_3 layer.

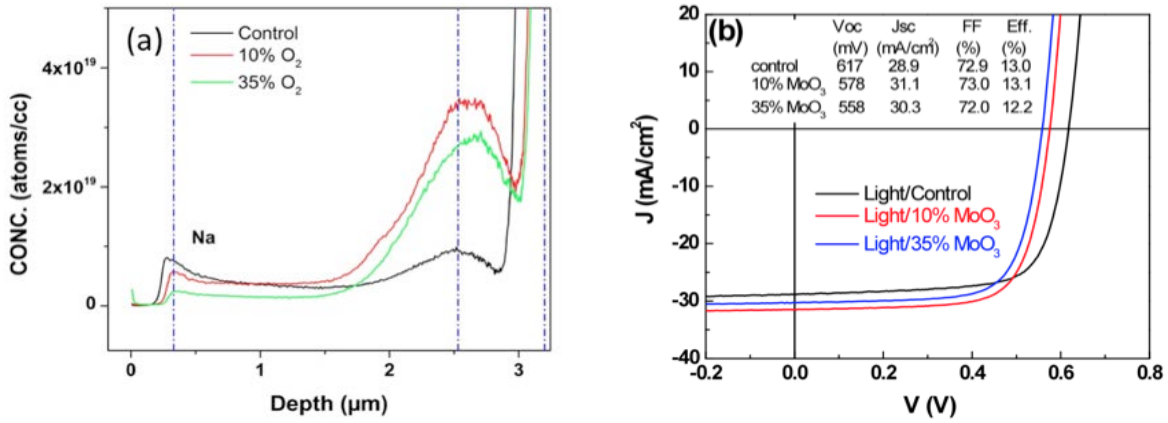

Figure 21. (a) SIMS depth profiles of Na in Cu(InGa)$(SeS)_2$ films with and without MoO_3 and (b) JV characteristics of CIGSS solar cells with or without MoO_3 layer.

The Cu(InGa)$(SeS)_2$ cells exhibit lower V_{OC} with increasing O_2 content, shown in Figure 21(b). For the 10% O_2 case the drop in V_{OC} may be bandgap related as a corresponding increase in J_{SC} is also observed. The lower V_{OC} without increased J_{SC} at 35% O_2 suggests that suppression of Na diffusion causes the loss of device performance. While

modifications to the process including extrinsic Na incorporation might enable comparable performance with the MoO_3 layers, no significant benefit was observed.

Task #2: Precursor Structure and Reaction

This task focused first on developing a baseline process for control of composition gradients and reaction pathways as described in the section of Process Description above. The second focus was on modifications to that process to improve device performance, enhance reaction rates and, using a Se-capped precursor, develop a process for reaction that eliminates the use of H_2Se.

Reaction S-termination

Control of the through-film relative Ga gradient was a major objective. A second issue related to the composition was determining the role of the S incorporated at the end of the process. To characterize the S-termination, processes using reaction with either H_2Se or H_2S as the final step of a three-stage reaction process were compared [23].

The baseline reaction was used for these experiments except for the use of H_2Se in the 3rd-step. The resulting films had similar reaction characteristics including the intermixing of the Ga, elimination of the InSe phase, and grain size enhancement regardless of the hydride gas. One difference was that the 3rd-step H_2Se reaction resulted in a coarser surface morphology. Atomic force microcopy characterization showed that the rms roughness was about 70% higher than with the baseline the 3rd-step H_2S reaction [23].

The most significant difference in the films was the composition near the surface as shown in Figure 22. The 3rd-step H_2Se reaction induced surface Ga depletion after the Ga homogenization in the 2nd-step Ar anneal and is likely a consequence of the preferential reaction of In–Se over Ga–Se [8]. Thus, in order to maintain the homogeneous Ga profile, a 3rd-step sulfization is a better option for completing the reaction. However, the 3rd-step H_2S reaction induced a half-micron deep sulfur incorporation. Not shown here, there was no significant difference in the depth profiles of Na, which diffused from the soda lime glass substrate, in the fully reacted samples.

To note the effects of S and Ga on the bandgap, band profiles were calculated according to the composition-bandgap relationship from ref. 24 and are also shown in Figure 22. The estimated minimum bandgaps of the CIGS film and CIGSS film are 1.05 eV and 1.16 eV, respectively. Increased Ga content primarily raises the conduction band minimum (CBM) while increased S raises the CBM and also lowers the valence band maximum (VBM) [25,26]. The method to determine the positions of the CBM and VBM in contrast to a reference level (e.g. vacuum level) using the compositional data as described in ref. 23. As seen, the CBM in the 0.2 μm top CIGSS surface is likely to be increasing toward its front surface. The increase in the CBM near the film surface due to S uptake in the CIGSS film can create a barrier to electron transport. In contrast, the CIGS cell with the 3rd-step H_2Se reaction film does not have S on the surface and the Ga depletion near the top surface might be benign in terms of electron transport.

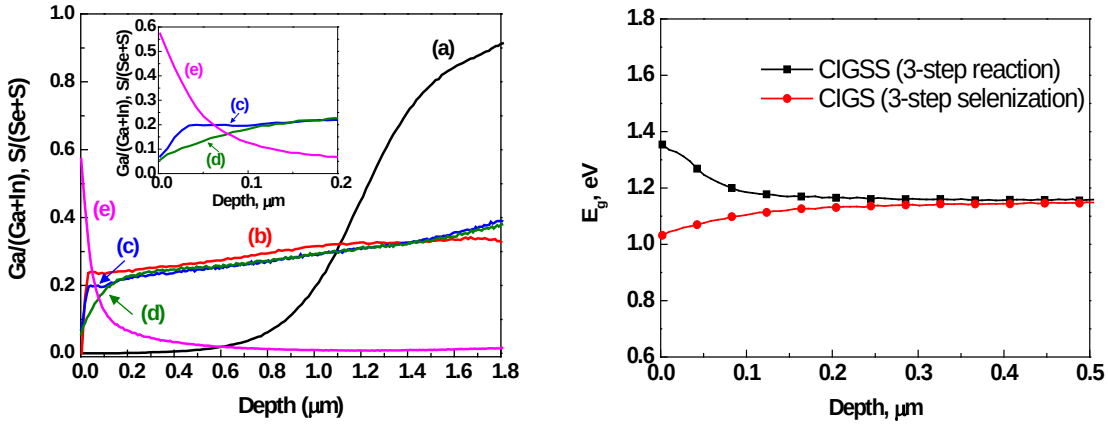

Figure 22. (Left) Ga/(Ga + In) ratios after (a) 1st-step selenization, (b) 2nd-step Ar anneal, (c) 3rd-step sulfization (H_2S reaction), and (d) 3rd-step selenization (H_2Se reaction), derived from SIMS analysis. The S/(Se+S) ratio (e) is also shown for the three-step reaction with S. The inset figure shows the Ga/(Ga + In) and S/(Se+S) profiles near the front surface. (Right) bandgap profiles calculated [24] of CIGS and CIGSS films using 3rd-step reactions with S and with Se.

Solar cells were fabricated from the reacted films and their J–V curves and characteristics are shown in Figure 23 and Table 5. The baseline cell had an efficiency η = 14.4% with V_{OC} = 609 mV, while the cell with the 3rd-step H_2Se reaction had a lower V_{OC} and FF. The diode quality factor (A), series resistance (R_S) and shunt conductance (G) were determined by diode analysis of dark JV data [27] and are also listed. A higher diode quality factor appears to be main cause of the poor FF of the cell with the three-step selenization.

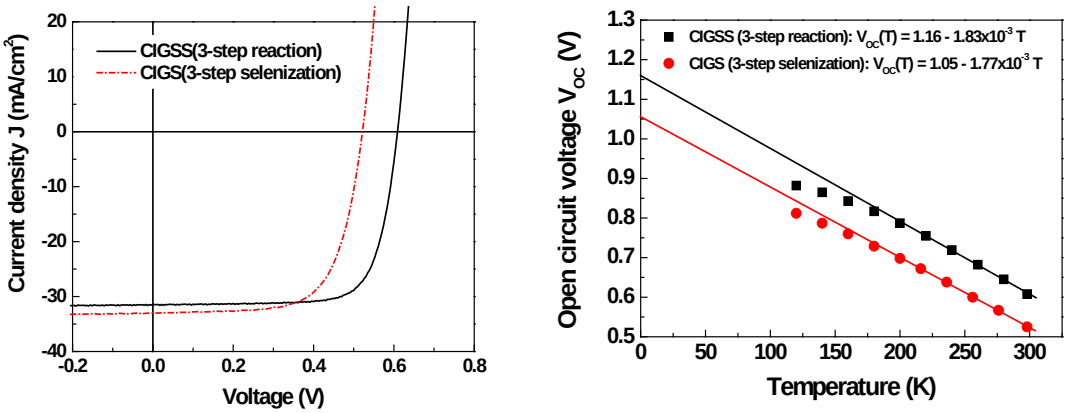

Figure 23. (Left) Light JV curves of CIGS and CIGSS solar cells with three-step reaction (solid black) and three-step selenization (dashed red) films. (Right) V_{OC}-T plots of CIGSS and CIGS cells. The activation energy of recombination in the CIGSS and CIGS solar cells are 1.16 eV and 1.05 eV, respectively.

It should be noted that the V_{OC} of the cell with the 3rd-step H_2Se reaction is lower than that expected from its bulk Ga content, suggesting that the V_{OC} is controlled largely by the Ga content of the top 0.1 μm thick layer. Temperature-dependent V_{OC} (V_{OC}-T) measurements were performed to determine the activation energy of recombination in

each cell in an attempt to understand the lower V_{OC} of the cell with the three-step reaction, as shown in Figure 23(right). The activation energy for recombination (E_a) is determined from the y-intercept of V_{OC} vs. T. The CIGSS (with 3rd-step H_2S reaction) and CIGS (with 3rd-step H_2Se reaction) cells had E_a = 1.16 eV and 1.05 eV, respectively. These activation energies are comparable to their minimum bandgaps, an indication that the dominant recombination in each cell takes place around the narrowest bandgap. Therefore, the surface Ga depletion in the CIGS apparently limits V_{OC} and the primary benefit of H_2S reaction is to control the near surface composition.

Table 5. JV parameters of cells shown in Figure 23.

Sample	η %	V_{OC} mV	J_{SC} mA/cm^2	F.F %	A	R_S Ωcm^2	G mS/cm^2
3-step reaction	14.4	609	31.5	75.1	1.4	0.3	0.2
3-step selenization	11.7	522	33.0	68.1	2.0	0.3	0.8

Ag Incorporation - Precursor

Results described in Task 1 showed promising benefits with Ag alloying including more homogeneous precursor morphology attributed to reduction of the elemental In phase, improved adhesion of reacted films enabling higher temperature reaction, and possibly faster reaction times. So to expand the study of Ag alloying a Ag-Ga sputter target was purchased allowing complete variation of the Ag/Cu ratio while fixing the Ga/(In+Ga) and (Ag+Cu)/(In+Ga) composition ratios.

To study Ag-alloying in the precursors, six different sets of Ag-Cu-Ga-In metal precursors were deposited onto Mo-coated soda-lime glass substrates by dc magnetron sputtering at room temperature using $Cu_{0.77}Ga_{0.23}$, $Ag_{0.77}Ga_{0.23}$, and In targets [28]. Sample A was prepared by co-sputtering of Cu-Ga and In layers on a rotating substrate to give ~700 alternating layers [10], as described on page 9. Sample B incorporated a 70 nm thick Ag-Ga layer on Mo followed by similar co-sputtered Cu-Ga and In layers. Samples C to F were deposited by sputtering different layer-by-layer sequences of Cu-Ga, Ag-Ga, and In. These sequential processes are compatible with an in-line process as it would likely be deposited for manufacturing. Sputtering sequences and composition of the samples are summarized in Table 6. The results of samples A-C as presented in the previous report are also included here for comparison reasons. The effect of different sputtering sequences on the structural properties of the Ag-Cu-Ga-In metal precursors and on the selenized films were studied using XRD and SEM. The correlation with device properties is addressed. Sputtering parameters were chosen to result in Ag/(Cu+Ag) ≈ 0.25 and (Ag+Cu)/(Ga+In) ≈ 0.90.

Figure 24 shows plan-view and cross-sectional SEM images of the various metal precursors. Figure 25 shows the XRD analyses of the metal precursors including the phases identified for each condition. As previously shown, the co-sputtered Cu-Ga-In precursors (Figure 24(a)) contain large nodules on the surface of the film. XRD results shown in Figure 25 confirm the presence of In, CuIn, and $Cu_9(In,Ga)_4$ phases.

Table 6. Sputtering sequences and compositions of the precursors.

Sample	Sequence 1	2	3	Composition by XRF (Ag+Cu)/(Ga+In)	Ag/(Ag+Cu)	Ga/(Ga+In)
A	Cu-Ga + In	–	–	0.94	0.00	0.25
B	Ag-Ga	Cu-Ga + In	–	0.80	0.28	0.20
C	Ag-Ga	Cu-Ga	In	0.90	0.25	0.23
D	Ag-Ga	In	Cu-Ga	0.91	0.23	0.23
E	Cu-Ga	Ag-Ga	In	0.96	0.26	0.24
F	Cu-Ga	In	Ag-Ga	0.80	0.26	0.21

Incorporating an 85 nm Ag-Ga layer underneath the Cu-In-Ga layer (sample B) modifies the morphology of the precursor. There are no signs of a nodular structure indicating less agglomeration of In. The SEM cross-section image also shows a uniform structure and the XRD pattern shows no indications of a metallic In phase. Instead, Ag(In,Ga)$_2$, CuIn, and Cu$_9$(In,Ga)$_4$ phases are observed. The formation of an Ag-In intermetallic phase is known to be a diffusion-controlled process. Ag and In interdiffuse when deposited in a vacuum atmosphere [29].

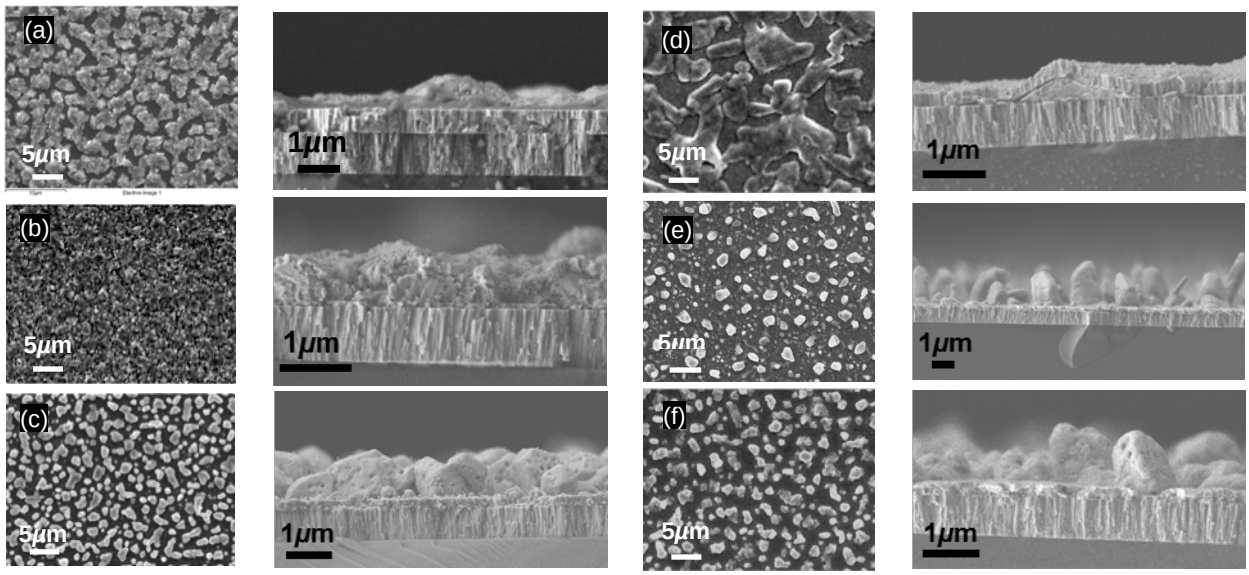

Figure 24. Plan-view/cross-sectional SEM images of the precursors (a) Mo/Cu-Ga-In, (b) Mo/Ag-Ga/Cu-Ga-In, (c) Mo/Ag-Ga/Cu-Ga/In, (d) Mo/Ag-Ga/In/Cu-Ga, (e) Mo/Cu-Ga/Ag-Ga/In, and (f) Mo/Cu-Ga/In/Ag-Ga.

Sample C with Mo/Ag-Ga/Cu-Ga/In stacked layers shows the formation of In-rich islands on an Ag-Cu-In-Ga background. The SEM cross-section image illustrates up to ~1 μm high In-rich agglomerates formed on the precursor's surface. XRD analysis shows that the presence of a Cu-Ga layer between the Ag-Ga and In layers hinder the formation of Ag(In,Ga)$_2$ phase. Instead, elemental Ag and In metallic phases are detected.

In sample D, the In layer deposited between the Ag-Ga and Cu-Ga layers alters the morphology of the precursor to an irregular island orientation. The SEM cross-section

image indicates that the islands consist of ~400 nm thick mixed Ag-Ga-In nodules covered by a ~200 nm Cu-Ga layer. Spot-EDS analyses (in plan-view mode) showed that the nodules consist of Cu-Ga-Ag-In while Ag is not identified in the background. The XRD pattern in Figure 25 reveals a similar phase structure to that observed in sample B, only with higher Ag(In,Ga)$_2$ peak intensities.

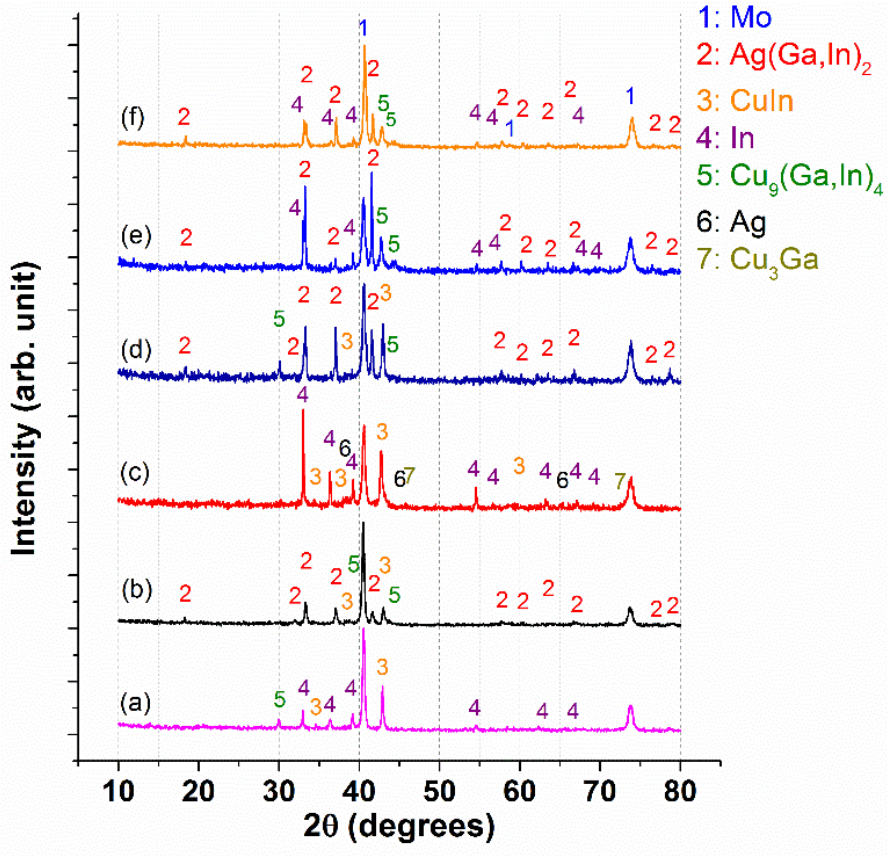

Figure 25. XRD patterns of precursors (a) Mo/Cu-Ga-In, (b) Mo/Ag-Ga/Cu-Ga-In, (c) Mo/Ag-Ga/Cu-Ga/In, (d) Mo/Ag-Ga/In/Cu-Ga, (e) Mo/Cu-Ga/Ag-Ga/In, and (f) Mo/Cu-Ga/In/Ag-Ga.

Samples E and F were deposited with a Cu-Ga layer followed by alternating Ag-Ga and In layers. In sample E, with a Cu-Ga/Ag-Ga/In sequence, the Ag-Ga and In layers are not intermixed, leading to the formation of ~2.5 µm high nodules that mostly (95 %) consist of In and which are presumably formed by the Stranski-Krastanov (S-K) type growth mode [30]. Sputtering the Ag-Ga layer on top of an In layer (sample F) leads to the formation of ~1 µm high nodules. Spot-EDS results (in plan-view mode) indicate that the nodules have a lower amount of In and a higher amount of Ag compared to those in sample E. In samples E and F, Ag is generally not present in its elemental state but rather within the Ag(In,Ga)$_2$ phase. Furthermore, both of the structures E and F contain elemental In.

Reaction of the films to form ACIGS was completed with a 1-step reaction. The reactor was first ramped up to 450ºC in 20 min in flowing 0.0035% O_2/Ar. Then the H_2Se gas

flow was started. After 10 min, samples were pushed into the hot zone and held for 50 min. Then the samples were pulled out from the heated zone and cooled down to room temperature in Ar flow. As shown in Figure 26 and Table 7, the highest overall performance was achieved in sample F with V_{OC} = 0.52 V, J_{SC} = 38.2 mA/cm^2, FF = 76.4 %, and an efficiency = 15.2%, made from the Cu-Ga/In/Ag-Ga metal precursor and without AR-coating. This structure was therefore selected for further experiments below on reaction studies.

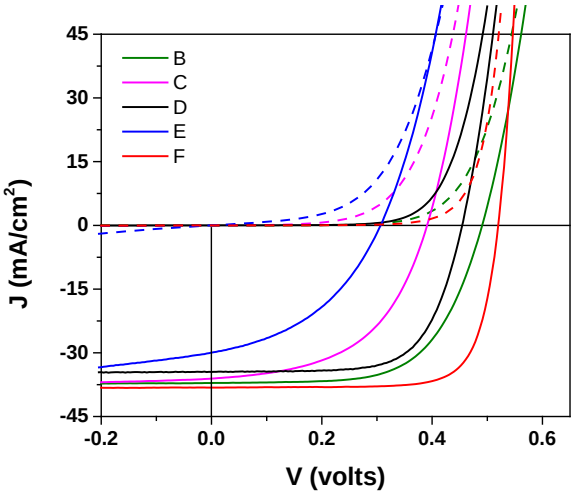

Figure 26. J-V characteristic after device fabrication of samples B-F. Dark and light J-V curves indicated by dashed and solid lines, respectively.

Table 7. EDS of top surface of the films after selenization and the related device characteristics.

Sample	Composition Ratios				Device Results			
	(Ag+Cu)/ (Ga+In)	Ag/ (Ag+Cu)	Ga/ (Ga+In)	Se/ Metals	V_{oc} (V)	J_{sc} (mA/cm^2)	FF (%)	Eff. (%)
B	0.95	0.29	0.04	1.03	0.44	33.7	61.9	9.2
C	1.02	0.23	0.11	0.99	0.39	36.1	51.8	7.3
D	1.03	0.24	0.07	0.98	0.45	34.5	67.5	10.6
E	1.09	0.26	0.13	0.96	0.31	30.0	41.9	3.9
F	0.99	0.25	0.08	0.97	0.52	38.2	76.4	15.2

Ag Incorporation – Phase Equilibrium Predictions

The substitution of Ag for Cu in the CIGS provides an additional degree of freedom to tune the properties of the absorber. The possibilities include increasing the bandgap energy, modifying precursor microstructure to reduce void formation, increasing the rate and/or decreasing the temperature of absorber synthesis, and modifying the reaction pathway. During selenization of metal precursors the metals react slowly with Se, limited predominantly by diffusion. Thus as temperature of the precursor is ramped during selenization, there are regions of metal only that can undergo phase changes that significantly impact the final absorber (e.g., formation of the γ-Cu_9In_4 phase or a liquid phase to assist growth). To help guide the development of precursor structures and analysis of data, a full assessment of the phase equilibria and thermochemistry for this 4-component metal system was performed. The assessment was compared to

experimental equilibrium data and equilibrium reaction pathways were predicted. In addition, HT-XRD measurements were made on metal-only precursors to estimate departures from equilibrium.

The model is comprised of previously assessed binary models (Ag-Cu, Ag-Ga, Ag-In, Cu-Ga, Cu-In, and Ga-In) that were carefully chosen to be self-consistent, structure-based, and compatible. The small experimental dataset for Ag-Cu-Ga was well matched by symmetric extrapolation of its constitutive binary parameters (Figure 27(a)). The Ag-Ga-In system was assessed, and 3 new ternary parameters were optimized to predict the experimentally observed compositional range of $Ag_2(Ga,In)$. An isothermal slice of the assessed phase diagram at 550 K is shown in Figure 27(b). Previous Ag-Cu-In and Cu-Ga-In assessments were used without modification. The sparse Ag-Cu-Ga-In experimental data was well-predicted by the model, and calculations were performed to aid practical applications. As examples it was found that increasing Ag/I or annealing Ag-Cu-Ga-In precursor films would enhance liquid formation, compositional homogeneity, and reduce (In) formation.

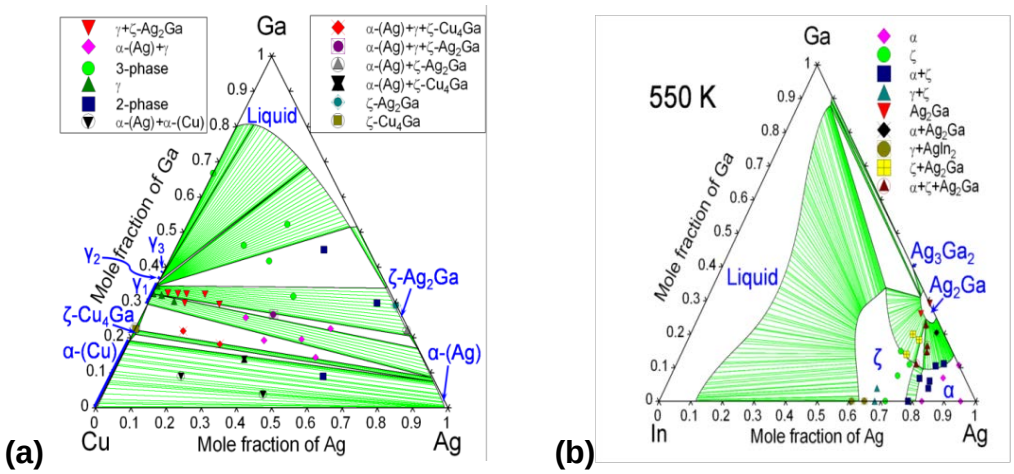

Figure 27. (a) Ag-Cu-Ga 723 K isotherm via Muggianu extrapolation of binary models, experimental data. (b) Calculated 783 K Ag-Cu-In isotherm from optimized model. Here 'γ' refers to γ-Cu_9In_4.

Constant I/III = 0.9 phase diagrams calculated at constant temperature were examined for trends. At 300 K, the phase diagram is dominated by the presence of many coexisting low temperature phases (*e.g.* Ag_2Ga, Ag_3Ga_2, $AgIn_2$, $Cu_{11}In_9$, $CuGa_2$, and In). At 500 K, the diagram is simpler, with the γ+ζ+L three-phase region occupying about half of the area. At 700 K, the constant I/III = 0.9 phase diagram is enveloped by the liquid phase on the Ag-rich side. This calculated diagram demonstrates how adding Ag to traditional Cu-Ga-In precursor films represents a practical route to enhance elemental inter-mixing (via faster atomic diffusion in the liquid) and improve wetting of the substrate. Figure 28 shows that as Ag/I is increased at 700 K, the amount of liquid increases substantially. For achieving desirable composition distributions and phases prior to chalcogenization, Figure 3 demonstrates that increasing Ag/I and temperature both lead to more liquid that is Ag and Ga-rich. This indicates that there may exist an

optimal trade-off for increasing Ag/I composition and increasing annealing temperature for ACGI precursor films

More common T-x phase diagrams were calculated by fixing the composition to the extent that only 2 degrees of freedom remain. An example at constant I/III = 0.9 and Ga/III = 0.25 is shown in Figure 29. Although there are complicated phase relationships in the diagram, one feature of practical interest is the change in phase existence near Cu/(Ag+Cu) = 0.65. At low temperature, metal precursors would contain elemental In for Cu/(Ag+In) > 0.65, but not for Cu/(Ag+In) < 0.65. Avoiding or reducing In agglomeration on the surface of precursors may be a route to increasing compositional homogeneity, which is desirable during chalcogenization. The thermodynamic calculations shown in Figure 29 indicate that increasing Ag/(Ag+In) to 0.35 or greater would consume In, which could homogenize composition in real precursor films.

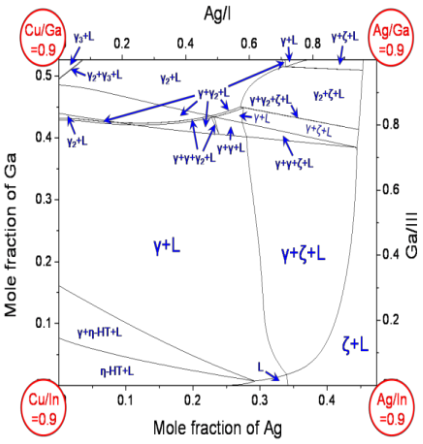

Figure 28. Calculated constant I/III = 0.9 phase diagram at 700 K. Here 'γ' refers to γ-$(Ag,\underline{Cu})_9(Ga,In)_4$, '$\gamma_2$' refers to γ_2-Cu_9Ga_4, and 'γ_3' refers to γ_3-Cu_9Ga_4.

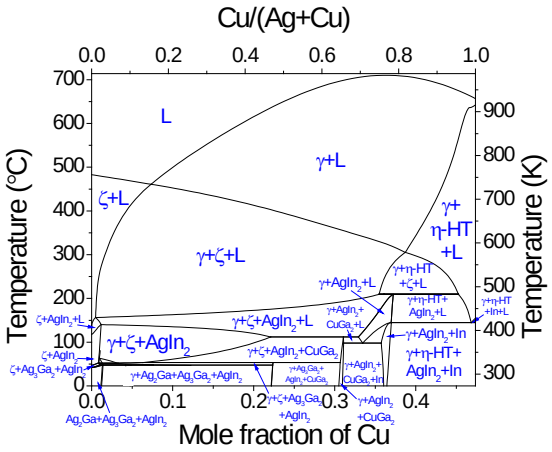

Figure 29. Calculated ACGI phase diagram with constant I/III = 0.9 and Ga/III = 0.25. Here 'γ' refers to γ-$(Ag,\underline{Cu})_9(Ga,In)_4$.

In this work, for the first time, a self-consistent thermodynamic database for the Ag-Cu-Ga-In material system has been assembled and assessed that predicts the phase diagrams well. Equilibrium models predict that either increasing Ag/Cu+In ratio or annealing ACGI precursor films would enhance liquid formation and reduce formation of the γ-$(Ag,\underline{Cu})_9(Ga,In)_4$ phase, believed responsible for Ga segregation. Substitution of Ag should reduce In agglomeration on the surface.

Ag Incorporation – Reaction Pathways

Experiments have been performed to determine the chemical reaction pathways to formation of (Ag,Cu)(In,Ga)Se_2 using time-progressive *ex-situ* atmospheric pressure H_2Se reactions. In order to have high temperature ramp rate, the experiments were performed using a rapid thermal processing (RTP) modification to our reactor as shown in Figure 30. Previously, a heat-jacket was used – this gives a substantially slower ramp rate than the RTP lamp. Figure 30 also compares a sample's temperature immediately after being pushed into the hot zone of the heat-jacket (450ºC) with sample heated to 450ºC under the lamp. As the inset figure shows, it takes about 2 seconds for the RTP

system to ramp up to the defined temperature compared to more than 5 minutes using the heat-jacket.

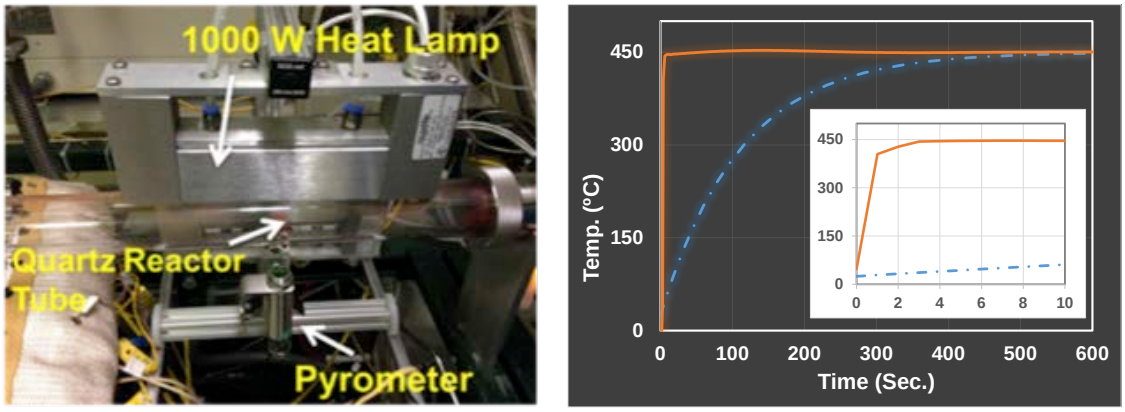

Figure 30. (left) RTP system used to perform the *ex-situ* experiments, (right) temperature's profile of a sample using RTP process (solid line), and heat-jacket (dashed line) for a maximum temperature of 450ºC.

In the RTP process, the reactor was charged with 2% H_2Se/Ar gas. Then the sample ramped up to T = 450ºC and reactions were performed at different times of 2, 3.5, 5, 10, 20, and 45 minutes. Then the lamp was turned off and samples cooled down to the room temperature in Ar flow in ~ 1 minute. Resulting films were analyzed using SEM, XRF and XRD/GIXRD to explore the morphology, composition and phase formation after each step. Here, we started the reaction pathway analysis for precursors with Ag/(Cu+Ag) ≈ 0.25. Figure 31 shows the plan-view SEM images of samples selenized at 450ºC in the range of 2 - 45 minutes. As it is seen that the nodular morphology of the precursors is still appears after 2 minutes reaction. Figure 32 shows the relative Ga and Se compositions versus reaction time measured by EDS, which probes roughly the top half of the film, and XRF analysis which probes the entire film. Front-side EDS results show Ga grading occurs in the first 10 minutes reaction time. At that time, EDS (front-side) and XRF show Se/M ~0.93 and 1, respectively.

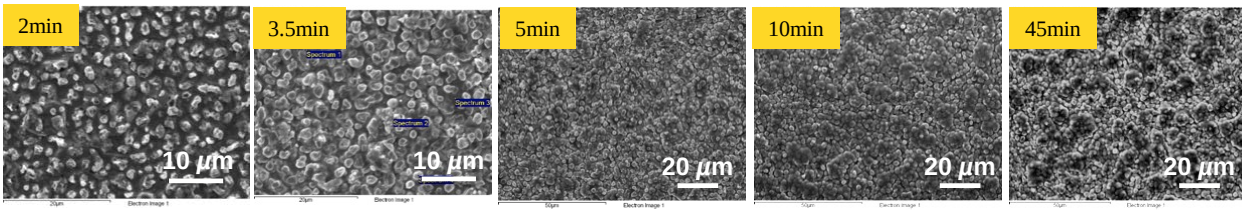

Figure 31. Plan-view SEM images of samples selenized at 450ºC at different times of 2, 3.5, 5, 10, and 45 minutes.

The ratio Se/M of the sample selenized at 450ºC for 2 minutes is less than 2% measured by XRF analysis. The XRD spectrum in Figure 33 of the sample is also similar to the one only annealed in Ar at 450ºC for 2 minutes. Both films show similar XRD peaks attributed to to In, (Ag,Cu)In_2, Cu_2In, $Cu_9(In,Ga)_4$ phases, though some of the peaks have not yet been identified. These suggest that significant reaction only initiated after 2 minutes.

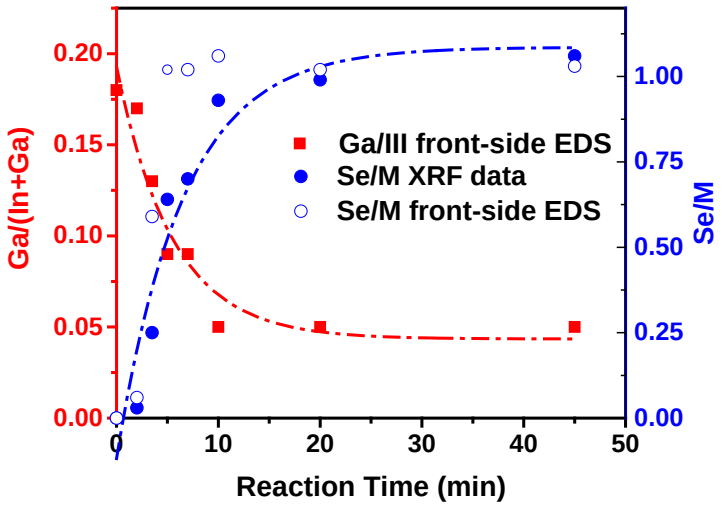

Figure 32. Ga and Se profile versus reaction time measured by EDS (front-side) and XRF analysis.

XRD spectra of the samples selenized for 3.5 minutes shows formation of InSe, In_4Se_3 and chalcopyrite phases. However, peaks attributed to In, (Ag,Cu)In_2, Cu_2In, $Cu_9(In,Ga)_4$ phase and unidentified peaks are still observed. The peak intensity of the chalcopyrite phase increased with further reaction up to 5 and 7 minutes along with disappearance of In and $AgIn_2$ and $Cu_9(In,Ga)_4$ phases. However, the InSe, Cu_2In phases and the unidentified peaks still exist in those samples (Figure 34). XRD patterns show that the chalcopyrite phase fully formed after 10 minutes reaction time (Figure 35).

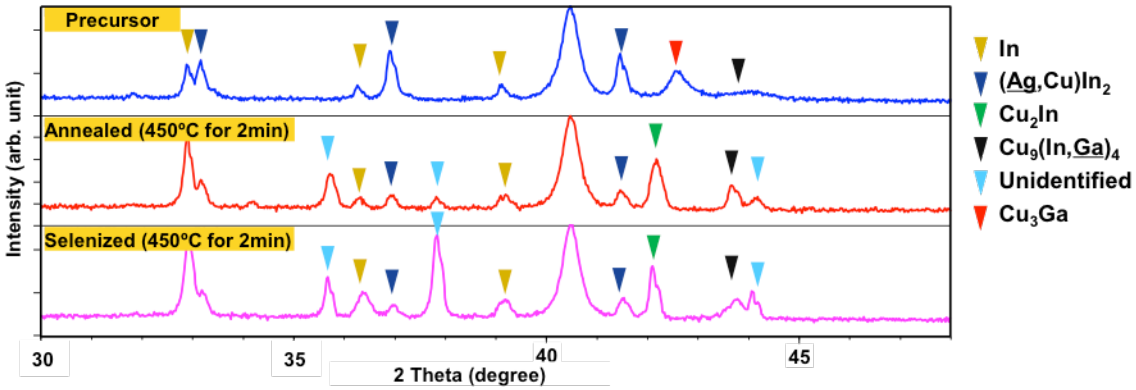

Figure 33. Comparing the XRD graphs of the precursor, annealed and selenized samples at 450ºC for 2 minutes.

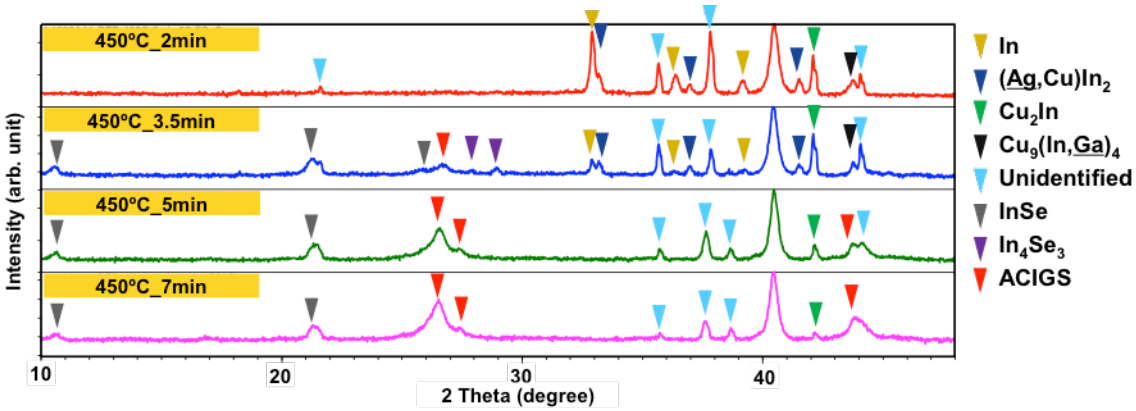

Figure 34. XRD graphs of selenized samples at 450ºC for 2, 3.5, 5, and 7 minutes

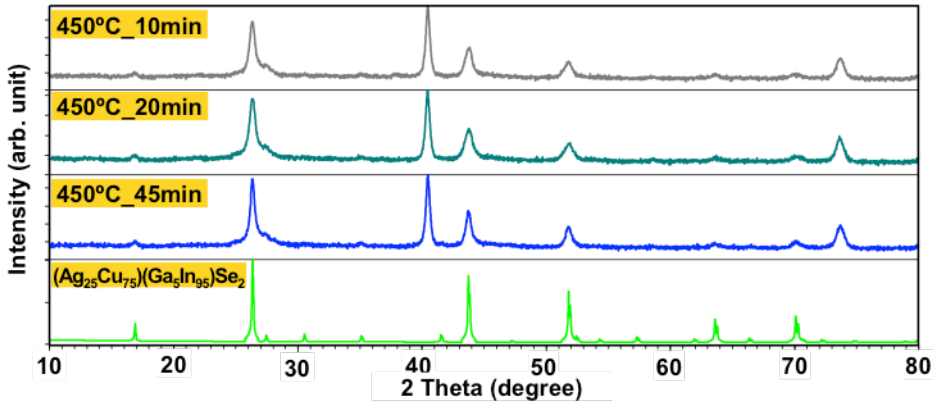

Figure 35. XRD patterns of selenized samples at 450ºC for 10, 20, and 45 minutes compared to simulated powder distraction pattern of $(Ag_{25}Cu_{75})(Ga_5In_{95})Se_2$ phase.

In-situ identification of reaction pathways and estimation of product formation rates via HTXRD provides additional insight into absorber synthesis and suggests process improvements. Reaction pathways were identified by observing phase transformations from diffraction patterns taken between incremental temperature increases during selenization. Quantitative product formation rates (e.g. chalcopyrite formation) were estimated by measurement of chalcopyrite peak area increases in XRD spectra during isothermal selenization.

The effects of Ag alloying in CIGS was further investigated by selenizing three precursors with different Ag/(Ag+Cu) (listed in Table 8) but with the similar structure of SLG/Mo/Ag-Ga/In/Cu-Ga and similar (Ag+Cu)/(Ga+In) and Ga/(Ga+In). The phase evolution during selenization for each sample is shown in Figure 36. The results show that ~450°C is the Ag-Cu and/or Ga-In alloying temperature for ACIGS phases of different alloying compositions. Rapid Cu and/or Ga alloying into the chalcopyrite phase was observed at ~450°C in all three samples. ~500°C appears to be onset temperature of ACIGS decomposition. A gradual decrease in chalcopyrite peak area was observed in the two samples with higher Ag/(Ag+Cu) that began at ~500°C.

All three precursors appeared to follow the general pathway of

$$Ag(Ga_xIn_{1-x})_2 + \gamma\text{-}(Cu_yAg_{1-y})_9(Ga_zIn_{1-z})_4 + Se \rightarrow ACIGS.$$

Ga alloying in In-rich $Ag(Ga_xIn_{1-x})_2$ starting from 150°C until chalcopyrite formation at 230°C in precursor with lower Ag/(Ag+Cu) (precursor 1 and 2 in Figure 36). In the precursor with high Ag/(Ag+Cu) (precursor 3) In-rich $Ag(Ga_xIn_{1-x})_2$ decomposed at 150°C.

Table 8. Ag-bulk precursors and their overall composition 'Ag-Ga' and 'Cu-Ga' indicate sputtered deposited layer using an $Ag_{0.77}Ga_{0.23}$ target and a $Cu_{0.77}Ga_{0.23}$ target, respectively.

Precursor #	Precursor Structure	I/III	Ga/III	Ag/I
1	SLG/Mo/Ag-Ga/In/Cu-Ga	0.91	0.23	0.23
2	SLG/Mo/Ag-Ga/In/Cu-Ga	0.95	0.23	0.50
3	SLG/Mo/Ag-Ga/In/Cu-Ga	1.01	0.24	0.73
4	Mo/Cu-Ga/In/Ag-Ga	0.8	0.2	0.26
5	Mo/In/Ag-Ga	0.60	0.14	0.00

In addition to the Ag-Ga/In/Cu-Ga precursor stack order, the selenization of a Cu-Ga/In/Ag-Ga (precursor 4 in Table 8) was also characterized due to its ability to achieve the most efficient ACIGS-based device of this project. The pathway during SLG/Mo/Cu-Ga/In/Ag-Ga selenization is shown in Figure 15. In this case, the chalcopyrite phase began to grow from selenization of $Ag(Ga_xIn_{1-x})_2$, $Cu_{1.81}In$, and/or Cu_4Ga (peak overlaps with that of $Cu_{1.81}In$) to form Ag_2Se, AgCuSe, and $\gamma\text{-}(Cu_yAg_{1-y})_9(Ga_xIn_{1-x})_4$ which slowly fuels growth of ACIGS. Two separate chalcopyrite regions of different composition formed at 240°C but proceeded to form a single composition by 310°C and remained compositionally uniform after cooling.

To gain a better understanding of the selenization of SLG/Mo/Cu-Ga/In/Ag-Ga, its reaction pathway was compared to the selenization of a simpler stacked precursor, SLG/Mo/In/Ag-Ga (precursor 5) in which Cu was absent. The data is shown in Figure 38. This shows that choosing the right Ag/(Ag+Cu) appears to be key to making compositionally homogeneous chalcopyrite. The absence of Cu resulted in clear segregation of chalcopyrite with different compositions (In-rich and Ga-rich) from chalcopyrite formation at ~260°C through 600°C. Alloying during SLG/Mo/Cu-Ga/In/Ag-Ga selenization was due to Cu substituting for Ag during $\gamma\text{-}(Cu_yAg_{1-y})_9(Ga_xIn_{1-x})_4$ growth or that Cu enables Ga substitution for In in $\gamma\text{-}(Cu_yAg_{1-y})_9(Ga_xIn_{1-x})_4$. The Ag and In rich $\gamma\text{-}(Cu_yAg_{1-y})_9(Ga_xIn_{1-x})_4$ does not shift during ramping in the absence of Cu. Since the γ phase typically selenizes to from chalcopyrite, early alloying of the γ phase may lead to absorber layers that are compositionally more uniform.

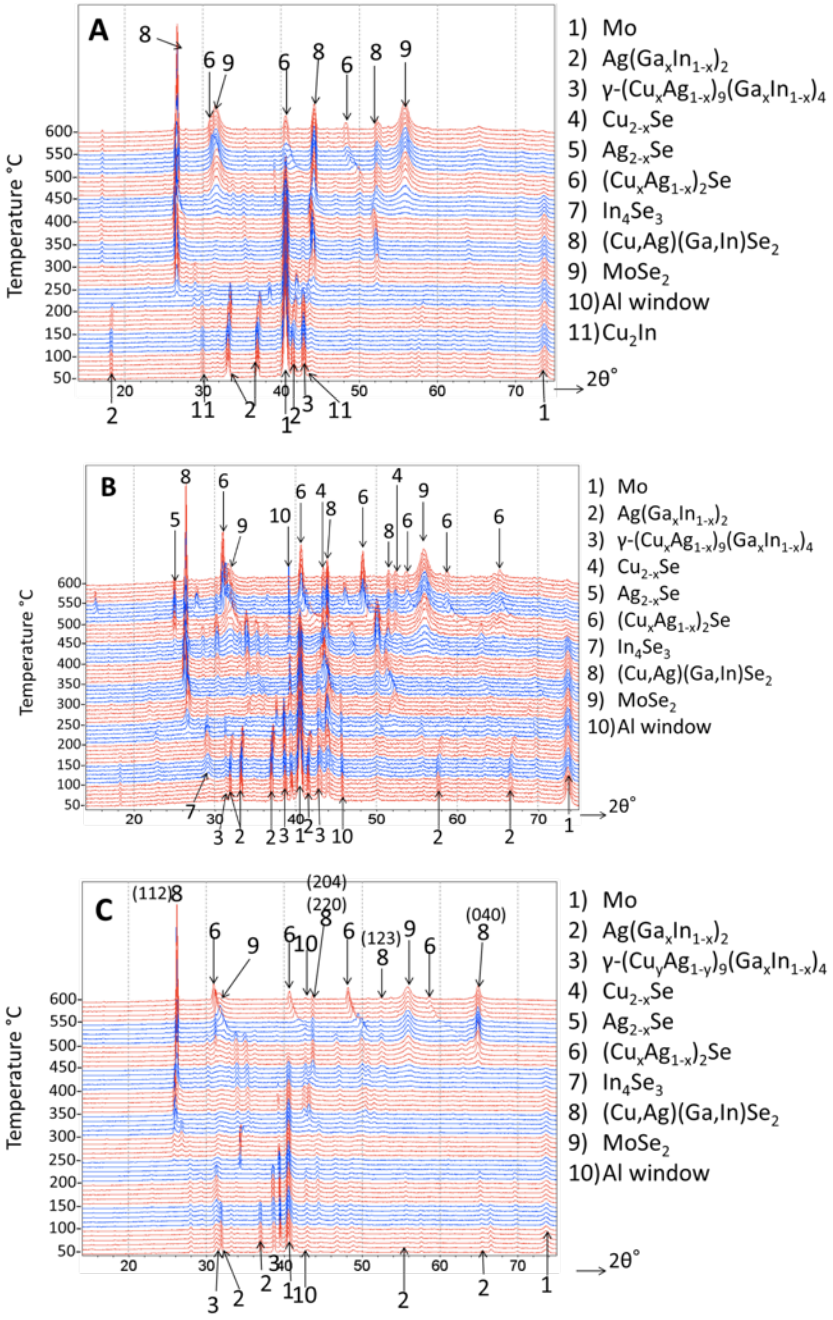

Figure 36. Temperature ramp selenizations of A) precursor 1, B) precursor 2, and C) precursor 3.

Through the analysis of a variety of sputter deposited advanced precursors from IEC, HTXRD was used to observe the reaction pathways during absorber layer synthesis and identify important process temperatures and process rates. This research provided insight into absorber precursor design, absorber compositional grading and homogenization, and absorber growth mechanism.

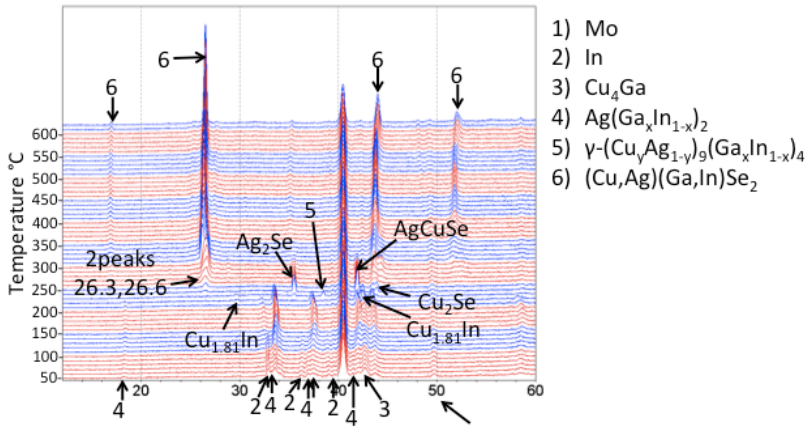

Figure 37. Temperature ramp selenization of precursor 4.

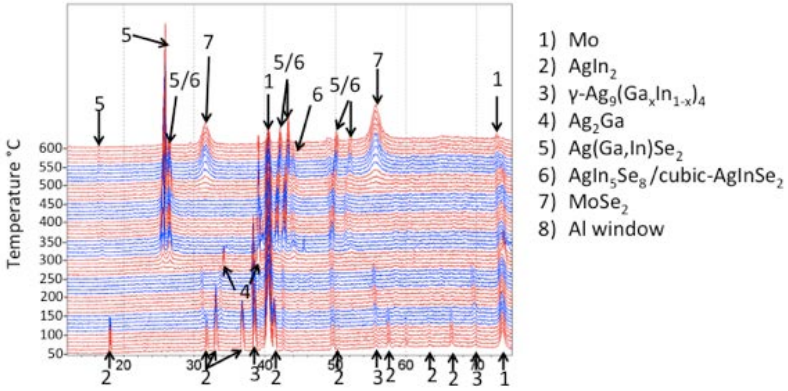

Figure 38. Temperature ramp selenization of precursor 5.

RTP Reaction of Se-Capped Precursors

An objective of the project is the reaction of a Se-containing precursor (Mo/Cu-In-Ga/Se) film using a one-step reaction process. This aims to minimize the reaction time while avoiding the use of toxic H_2Se. Both of these issues are of interest to industry as they seek to reduce production costs and improve safety. This approach is similar to the process AVANCIS uses for their thin films [31].

For this purpose, baseline IEC glass/Mo/Cu-Ga-In precursor samples were followed by evaporation of an elemental selenium layer [32]. The Se thicknesses were 6, 8, 10.5, and 12 µm. To form CIGSSe, the precursors were reacted using a two-step process under constant 1000 sccm Ar flow as shown in Figure 39 shows the temperature profile of the sample during the reaction. In the first step, the films react with the selenium capping layer. Reaction times ($t_{Se,Ar}$) of 7.5, 10, and 20 min are reported. The second step occurs in a 0.35 vol% H_2S diluted argon atmosphere to incorporate sulfur into the CIGS film. The length of the H_2S-step is fixed at 5 min. Table 9 lists the reaction conditions, composition, and adhesion of samples A to F which were reacted at varying Se reaction times in Ar ($t_{Se,Ar}$) and with Se-layers of varying thickness. The results are

compared to control samples from a 90 min long IEC three-step $H_2Se/Ar/H_2S$ reaction of uncapped precursors.

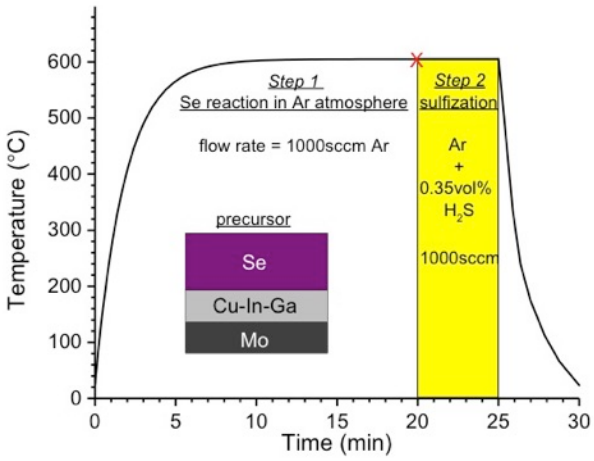

Figure 39. Temperature profile of the reaction process.

Figure 40 shows comparisons between the morphology of the front ((a) and (c)) and back sides ((b) and (d)) of the control sample obtained using the 90 min IEC baseline process [3] and of sample C of this study. The front and back sides of all samples A to F are comparable to those of sample C. While the front side images (a) and (c) show similar morphologies, the back side of the absorber layers fabricated in the present study (d) are almost free of voids, unlike the back interface of the control sample (b). It is hypothesized that the void formation is suppressed due to accelerated selenization of the metallic precursor, which may outpace the agglomeration of the intermetallics at the back contact.

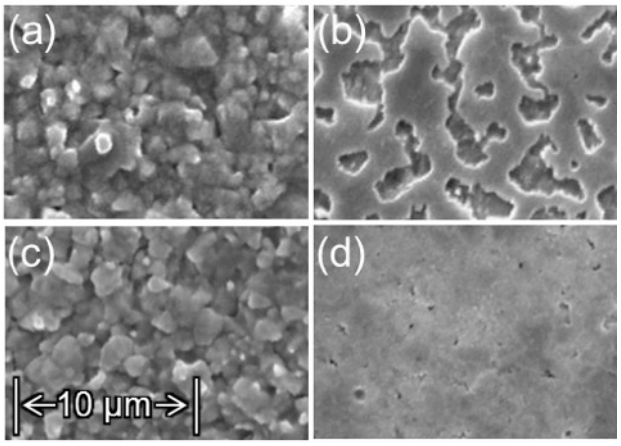

Figure 40. SEM images as measured from the (a) front side and (b) back side of the control sample compared with (c) front side and (d) back side SEM images from sample C.

Quantification of adhesion between the absorber layer and the Mo back interface was performed using the pull-test described above and the results [32] are included in Table 9. In this test a 16 mm^2 metal pin is glued to surface, the force to pull off the pin is measured, and the average of 10 tests on two samples used to determine adhesion. The control sample was easily peeled off to give adhesion = 6 ± 5 N/mm^2. Samples A to

D gave adhesion forces ranging from 17 to 32 N/mm^2 The improved adhesion might be a result of the reduced void density.

Table 9. Summary of performed reactions, sample composition, and adhesion. EDX measurements were performed on the front side (FS) and on the back side (BS) of the absorber.

Sample	Se thickness (µm)	$t_{Se,Ar}$ (min)	Side	Composition Cu/ (In+Ga)	Ga/ (In+Ga)	S/ (S+Se)	Adhesion (N/mm^2)
A	6	20	FS BS	1.01 0.94	0.17 0.34	0.07 0.00	≥ 23 ± 8
B	8	20	FS BS	0.96 0.94	0.13 0.43	0.07 0.06	≥ 32 ± 10
C	10.5	20	FS BS	1.01 0.92	0.11 0.43	0.05 0.08	≥ 20 ± 5
D	12	20	FS BS	0.95 0.89	0.09 0.41	0.05 0.09	≥ 17 ± 9
E	8	10	FS BS	0.97 0.92	0.16 0.38	0.05 0.02	n/a
F	8	7.5	FS BS	0.97 0.93	0.17 0.31	0.03 0.01	n/a
Control	IEC baseline three-step process [3] (90min)		FS BS	0.94 0.94	0.16 0.21	0.13 0.00	6 ± 5

As shown in Table 9, the Cu/(In+Ga) ratios are constant within the error of the EDS measurement ~ 0.95 from both the front side and back side, for all samples. The Ga/(In+Ga) and S/(S+Se) ratios however vary depending on the Se layer thickness (see samples A to D) and $t_{Se,Ar}$ (see samples B, E, and F), respectively. The Ga/(In+Ga) ratio differs for all samples from FS to BS indicating a Ga gradient from the FS to the BS though the degree of this grading depends on the Se layer thickness. Figure 41 shows these Ga-gradients as obtained from SIMS depth profiles. The gradient is largest for sample C and becomes smaller with shorter $t_{Se,Ar}$ and thinner Se layers, with the flattest Ga-grading observed in sample A with the 6 µm thick Se layer. The amount of sulfur accumulated at the back side of the absorber is dependent on $t_{Se,Ar}$ and whether the sample is under- or fully selenized after the first step, while the front side sulfur incorporation is correlated to the Se layer thickness. Overall, a longer reaction in Ar atmosphere leads to the more sulfur in the film, especially at the back interface.

XRD results in Figure 42 measured after just the Se reaction step in Ar atmosphere show that the 6 µm thick Se layer leads to an under-selenized film with $Cu_9(In,Ga)_4$ and InSe phases before the final sulfization step. The 12 µm thick Se layer, for example, leads to a completely selenized film with no intermetallic phases observed. Similar results indicating a complete reaction were observed for all samples B to F with Se thickness > 6 µm.

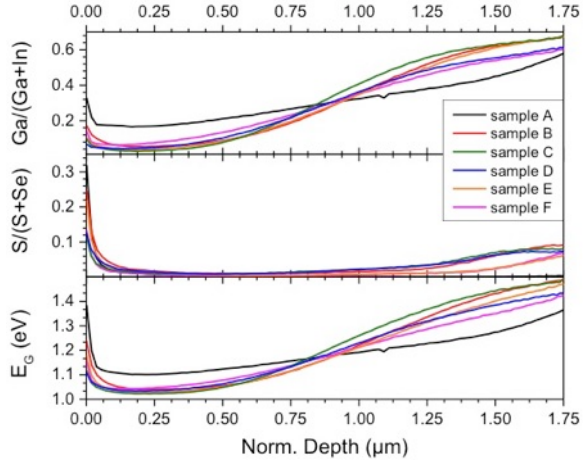

Figure 41. Band gap (E_G), Ga/(Ga+In), and S/(S+Se) depth profiles as calculated from SIMS measurements.

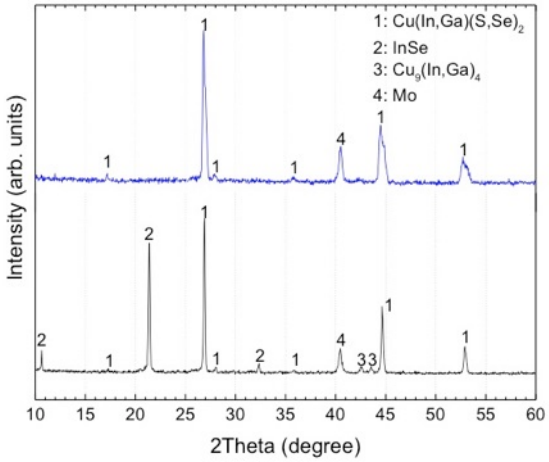

Figure 42. XRD patterns of films with a 12 μm (blue line) and 6 μm (black line) thick Se layer after just the Se reaction step in Ar (see X in Figure 1).

The compositional depth profile data was converted into through-film band gap (E_G) profiles [24] as shown in Figure 41. The flattest profile is obtained for sample A, where the amount of Se on the precursor was not sufficient to fully selenize the film in the first step. The minimum band gap obtained from this compositional measurement is ~ 1.10 eV. This value is slightly higher than that obtained from quantum efficiency measurements [32]. The minimum band gaps obtained from SIMS measurements for samples B to F are all close to 1.03 eV corresponding to pure $CuInSe_2$ and agree well with E_G values determined from QE are listed in Table 10. The precursors of the films B to F all had sufficient selenium to be fully reacted at the end of the first reaction step and their band gap profiles are much steeper as a result of the Ga being confined to the back part of the film. This results from Ga being less mobile after the complete selenization in step 1. While the band gap profiles at the front are dominated by the different S contents as a result of different Se layer thicknesses, the band gap profiles towards the back of the films are dependent on both the Ga and S profiles which can be influenced by both the Se layer thickness and $t_{Se,Ar}$. Thus it is possible to engineer the band gap profile by adjusting the thickness of the Se capping layer and t.

Table 10 gives a summary of the device characteristics. The device with the best performance in this study is sample C with a power conversion efficiency of η = 13.0 % and obtained from a precursor with a Se layer thickness of 10.5 μm and reacted for $t_{Se,Ar}$ = 20 min in argon followed by a 5 min reaction in H_2S/Ar. This result is close to the efficiency reached with the control sample (η = 14.2 %), while the overall reaction time was reduced by more than 70 %.

The results shown in this work offer a pathway to reduce the total anneal and reaction time to less than 25 min by the use of a Se-capped metallic precursor, avoiding the use of toxic H_2Se. Compared to our previous IEC baseline, where a typical reaction of an uncapped metal precursor required a minimum of 90 min, this represents a reduction of

at least 70 %, while still reaching photovoltaic conversion efficiencies of 13 %. It is suggested that the thickness of the selenium layer in the precursor has the biggest impact on the device performance, with an optimized Se layer thickness of 10.5 µm. It is further shown that the choice of the Se layer thickness and the time of the Se reaction step in Ar atmosphere can be useful tools to engineer the through film composition, mainly the Ga- and S-profiles, and hence the band gap profiles of reactively processed CIGSSe absorber layers. Additionally, the process presented in this work avoids the formation of voids at the Mo/CIGSSe interface almost completely and furthermore significantly improves the adhesion of the CIGSSe film at the Mo/CIGSSe interface.

Table 10. Summary of the J-V-characteristics for the best devices with RTP Reaction of Se-Capped Precursors.

Sample	Se thickness (µm)	$t_{Se,Ar}$ (min)	η (%)	V_{OC} (mV)	J_{SC} (mA/cm^2)	FF (%)	E_G (QE) (eV)
A	6	20	9.9	451	33.7	65.3	1.02
B	8	20	11.9	491	34.9	69.6	1.01
C	10.5	20	13.0	533	35.2	69.3	1.01
D	12	20	10.7	470	34.6	65.8	1.02
E	8	10	11.2	469	35.3	67.4	1.01
F	8	7.5	10.3	428	35.8	67.4	1.00
Control	IEC baseline 3-step.		14.2	599	32.2	73.5	1.09

To characterize the effects of the Se-cap on the reaction pathway during the annealing process, a SLG/Mo/Cu-Ga-In precursor with a 10.5 µm Se cap was investigated using HTXRD as shown in Figure 43 and the results were compared to the baseline SLG/Mo/Cu-Ga-In sample. Due to the thick Se-cap attenuating most of the incident x-rays, γ-$Cu_9(Ga_xIn_{1-x})_4$ and $CuSe_2$ were observed only after Se melted at 221°C. Beyond 221°C, however, the phase transformations were very similar except that the transformation temperatures were slightly lower for the Se-capped sample.

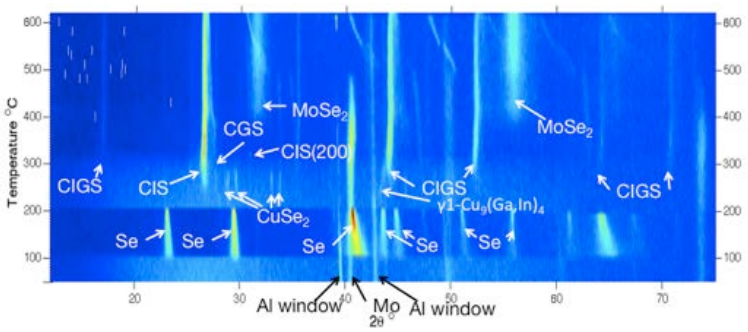

Figure 43. Temperature ramp of SLG/Mo/Cu-Ga-In/10.5 µm Se. Color temperature indicates the intensity of the peaks.

Figure 43 shows that CIS formed from γ-$Cu_9(Ga_xIn_{1-x})_4$ and $CuSe_2$ at ~240°C (~290°C for baseline sample). In for CIS formation was supplied by γ-$Cu_9(Ga_xIn_{1-x})_4$ decomposition with gradual peak shifting indicated the loss of In in γ-$Cu_9(Ga_xIn_{1-x})_4$.

CGS formed at ~340°C (~360°C for baseline sample). Excess liquid Se from the Se cap caused $CuSe_2$ to form instead of CuSe as predicted thermodynamically.
Ga-In alloying in CIGS increased with temperature but homogenization was not reached. Finally, CIS and CGS peaks merged during heating to 450°C, after which they remain CIGS phases of two different compositions (Figure 44).

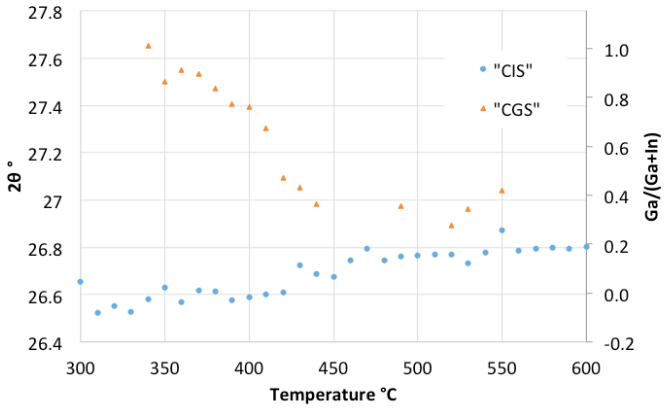

Figure 44. Peak positions (2θ°) and corresponding Ga/(Ga+In) ratio as a function of scan temperature during selenization. Two different compositions of $Cu(In_xGa_{1-x})Se_2$ were initially observed at ~ 290°C, one approximately pure $CuInSe_2$ (CIS).

IV. Conclusions

This project sought to provide pathways to improve module efficiency and manufacturability of CIGSS films using the reaction of metal precursors. Research goals included characterizing and controlling the Mo/CIGSS interface to improve adhesion and device characteristics, thereby increasing yield and module efficiency. For this purpose, the effects of interlayers Ag, Sb, Bi, and Te, on the Cu(InGa)$(SeS)_2$ interface were studied and a quantitative adhesion test was established. Also, the addition of Ag to the Cu-In-Ga precursor and its effect on the ACIGS film reaction was investigated. The project also developed an precursor structure containing Se and a reaction process to reduce processing time to 5 minutes and eliminate H_2Se usage, thereby increasing throughput and reducing costs.

Specific accomplishments of the project were:

- A three step $H_2Se/AR/H_2S$ reaction process was established, leading to a more homogeneous Ga distribution and control of $MoSe_2$ formation at the Mo/Cu(InGa)$(SeS)_2$ interface. The reaction pathway through this reaction process was characterized.
- The introduction of a thin Sb, Bi, or Te layer deposited on the Mo contact reduced inhomogeneity caused by In agglomeration in the Cu-Ga-In metal precursor and, with an Sb interlay, improved adhesion. With the Te interlayer, the density of voids in the reacted film was reduced but device showed no improvement.
- The addition of thin 5 - 32 nm Ag layer between the Mo and the Cu-Ga-Iin precursor creates a much more homogeneous precursor structure by minimizing agglomeration caused by formation of an elemental In phase. The Ag significantly improves adhesion of the reacted films enabling a broader process window including higher temperature without film delamination.
- Thermodynamic assessment showed that adding Ag to the baseline Cu-Ga-In precursor provides a practical route to enhance elemental inter-mixing (via faster atomic diffusion in the liquid) and improve wetting of the substrate.
- The effect of the H_2S reaction for the final reaction step was quantified. S is critical to control the surface composition and avoid Ga depletion in the CIGS which limits V_{OC} in devices.
- The capping of the Cu-In-Ga precursor with Se in order to avoid the use of H_2Se was shown to reduce the reactive annealing time down to 5 min to form single phase CIGS or ACIGS. This process can also significantly reduce void formation.

The project's statement of project objectives listed a set of results to be addressed. These are listed below by task and project phase. For each the outcome is cited with respect to this report or a publication.

Phase 1 - Task #1: Mo/CIGSS Interface

1. *A process for controlled incorporation of oxygen into the Mo surface.*
   As described from page 22, a reactively sputtered MoO_3 layer was used as an interlayer between the Mo contact and the Cu-Ga-In precursor.

2. *Reaction chemistry and kinetics of Se with Mo:O2 compared to standard Mo.*
   As described from page 22, the reaction of Se and CIGS reaction had no measureable effect on the growth of the precursor, CIGSS, or void formation. The MoO_3 layer did appear to reduce the formation of $MoSe_2$ but the was minimal because the 3-step baseline already process minimizes $MoSe_2$ formation. Na incorporation from the substrate was hindered.
3. *Cu-Ga-In precursor structures fabricated on Mo/interlayer substrates.*
   As described from pages 15 and 20, Ag, Sb, Bi, and Te interlayers were selected as candidate materials. Processes to deposit them between the Mo and Cu-Ga-In precursor using sputtering (Ag) or evaporation (Sb, Bi, Te) were developed

Phase 1 - Task #2: Precursor Structure and Reaction

1. *Description of the effects of reaction conditions in the H_2Se/H_2S process.*
   A detailed description of the reaction is given in sections from p. 10 and 24 and in refs. 8, 10. Processes to control the Ga gradient, enhance grain size, and minimize $MoSe_2$ formation were developed.
2. *Single phase $Cu(InGa)(SeS)_2$ formed by reaction of Cu-Ga-In-Se precursor in H_2S.*
   As described from page 37 and in ref. 32, using a Se-capped precursor allowed formation of single phase CIGSS using a high temperature anneal and 5 min. H_2S reaction.
3. *A reactor built to enable H2S reaction with well-defined short reaction times.*
   As shown in Figure 30, the hydride gas reaction was fitted with a quartz lamp heating system that enables heating to 450ºC in ~ 2 s.

Phase 2 - Task #1: Mo/CIGSS Interface

1. *Application of interlayers between the Mo and Cu-Ga-In precursor to suppress on void formation and control $MoSe_2$.*
   Detailed studies of Ag, Sb, Bi, and Te interlayers were carried out [14,19]. Ag interlayers had significant effects on precursor morphology and phase composition and improved adhesion to enable a wider reaction process window. A Te layer reduced void density and a Ab layer improved adhesion.
2. *Reaction pathway and kinetics of Se with Mo/interlayer structures.*
   This was not quantitatively addressed because the baseline reaction process minimized effects of Se reaction with the Mo [8], making characterization difficult.
3. *ACIGS films formed and the effect of Ag on the back interface determined.*
   As described from page 26 in in ref. 28, a novel Ag-Ga sputter target was used to characterize different and structures for Ag-Cu-Ga-In and a Cu-Ga/In/Ga/Ag-Ga structure was down-selected for reaction studies. Improved adhesion with Ag was demonstrated.
4. *A description of the effect of Na incorporation on the formation of voids, $MoSe_2$ and adhesion.*
   The effects of Na on the precursor reaction process were described in ref. [33].

Phase 2 - Task #2: Precursor Structure and Reaction

1. *Quantitative description of the effects of reaction conditions in the H_2Se/H_2S process.*

A detailed description of the reaction was extended to a quantitative characterization of the role of the S-reaction in the 3rd-step of the reaction as described in p. 24 and in ref. 23. The critical role of S in controlling the surface composition and it's effect on device behavior was determined.

2. *A process for formation of single phase CIGSS by 5 min H_2S reaction.* As described from page 37 and in ref. 32, a process to form single phase films was developed and characterized. The effect of the Se-capping layer thickness was determined and a 2-step anneal/H_2S reaction with 5 min hydride gas reaction was described.
3. *Description of the effect of Ag addition on reaction pathways to form ACIGSS.* Process and reaction characterization from page 31 identified important process temperatures and process rates and demonstrated that Ag-alloying in the precursor can be used to produce faster reaction rates and more homogeneous absorber films.
4. *Quantitative analysis of the effect of voids on CIGSS solar cells.* The effect of different process modifications on void formation was quantitatively determined. It was shown that the void density was not correlated to In agglomeration in the precursor or to adhesion in the reacted films. The void density can be significantly reduces by the reaction time/temperature profile.

The project objectives included a commitment to publish and present results openly. The following publications have resulted from this work:

1. "Three-step $H_2Se/Ar/H_2S$ reaction of Cu-In-Ga precursors for controlled composition and adhesion of Cu(In,Ga)$(Se,S)_2$ thin films" Kihwan Kim, Gregory M. Hanket, Trang Huynh, and William Shafarman*, Journal of Applied Physics*, **111**, 083710 (2012). DOI: 10.1063/1.4704390
2. "Three-step $H_2Se/Ar/H_2S$ Reaction of Metal Precursors for Large Area Cu(In,Ga)$(Se,S)_2$ with Uniform Ga Distribution" Kihwan Kim, Evan L. Kimberly, Andrew Damiani, Gregory M. Hanket and William N. Shafarman, *Proc. 38th IEEE Photovoltaic Specialists Conference* 1-6 (2012). DOI: 10.1109/PVSC-Vol2.2012.6656716.
3. "Characterization of (AgCu)(InGa)Se_2 Absorber Layer Fabricated by Selenization Process from Metal Precursor" Yuki Tauchi, Kihwan Kim, Hyeonwook Park and William Shafarman, *IEEE Journal of Photovoltaics*, **3**, 467-71 (2013). DOI: 10.1109/JPHOTOV.2012.2221083
4. "Incorporation of Sb, Bi, and Te Interlayers at the Mo/Cu-In-Ga Interface for the Reaction of Cu(In,Ga)$(Se,S)_2$" Kihwan Kim, Jaesung Han and William N. Shafarman, *Mat. Res. Soc. Symp. Proc.* **1538**, 15-20 (2013). DOI: 10.1557/opl.2013.999
5. "The effect of a high temperature reaction of Cu-In-Ga metallic precursors on the formation of Cu(In,Ga)$(Se,S)_2$" Dominik M. Berg, Christopher P. Thompson, William N. Shafarman, *Mat. Res. Soc. Symp. Proc.* **1538**, 3-8 (2013). DOI:10.1557/opl.2013.997

6. "H_2S reaction of Se-capped metallic precursors to form Cu(In,Ga)$(S,Se)_2$ absorber layers" Dominik M. Berg, Frank Cheng, William N. Shafarman, *Proc. 40th IEEE Photovoltaic Specialists Conference*, 323-27 (2014). DOI: 10.1109/PVSC.2014.6924923
7. "Effect of sputtering sequence on the properties of Ag-Cu-In-Ga metal precursors and reacted (Ag,Cu)(In,Ga)Se_2 films" Sina Soltanmohammad, Dominik M. Berg, Lei Chen, Kihwan Kim, Hamed Simchi, William N. Shafarman, *Proc. 40th IEEE Photovoltaic Specialists Conference*, 1707-1711 (2014). DOI: 10.1109/PVSC.2014.6925250
8. "Composition and bandgap control in Cu(In,Ga)Se_2-based absorbers formed by reaction of metal precursors**"** Kihwan Kim, Hyeonwook Park, Gregory Hanket, Woo Kyoung Kim and William Shafarman, *Progress in Photovoltaics*, **23**, 765**–**772 (2015). DOI: 10.1002/pip.2494.
9. "Na incorporation in Cu(In,Ga)$(Se,S)_2$ films grown on insulator-coated stainless steel foil using a metal precursor reaction" Kihwan Kim, Erten Eser and William N. Shafarman, *IEEE Journal of Photovoltaics* **5** ,1222–1228 (2015). DOI: 10.1109/JPHOTOV.2015.2435366

Two additional publications are in final preparation. In addition, ten presentations, including two invited presentations, at major technical conferences were made covering results from this project.

No patents were filed based on the project.

V. Budget and Schedule

This project was completed by the University of Delaware over the time period from 09/01/2011 to 5/30/2015. The total project budget was $1,200,000 with no cost share. There were total expenditures of $1,200,000. The original end date was 11/30/2014 and a no cost extension was granted making the end date 05/31/2015.

VI. Path Forward

This project has focused on developing a fundamental understanding of the process to form Cu(InGa)$(SeS)_2$ thin films for solar cells and modules using the reaction of metal precursors. This has lead to the development of a number of promising process modifications that could lead to improved manufacturing. IEC has had many discussions with US and foreign companies who use this process in the pilot or full manufacturing scale production of CIGSS modules. This also includes companies using co-evaporation or other hybrid processes which may benefit from some of the advancements demonstrated. This particularly applies to modifications to the back Mo/CIGSS interface and to S-treatment at the front surface. A specific future research objective will be to apply the findings of this work that allow control of the bandgap profiles through the film by controlling relative Ga and S profiles to improve device and module performance.

It is anticipated that these discussions will lead to formal collaboration either through direct interactions between the company and IEC or through joint application to DOE under future funding opportunities.

There are no direct commercialization or patent activities anticipated to result from this project.

VII. References

1. W.N. Shafarman, S. Siebentritt, and L. Stolt, Chapter 13 in *Handbook of Photovoltaic Science and Engineering, Second Edition*, ed. by A. Luque and S. Hegedus, John Wiley & Sons, Ltd., 546 (2011).
2. Nagoya Y et al., Solar En Mat. Solar Cells **67**, 247–253 (2001).
3. Probst V et al., Thin Solid Films **387**, 262–267 (2001).
4. V. Alberts, *Semicond. Sci. Technol.* **22**, 585 (2007).
5. H Sugimoto, Proc. *2014 IEEE 40th Photovoltaic Specialist Conference*, (2014).
6. G. M. Hanket, W. N. Shafarman, B. E. McCandless, and R. W. Birkmire, J. Appl. Phys.**102**, 074922 (2007).
7. In: JCPDS card No. 05-0642, Cu_3Ga: JCPDS card No. 44-1118: Cu_4In, JCPDS card No. 42-1477, Cu_9In_4: JCPDS card No. 42-1476, Cu_9Ga_4: JCPDS card No. 02-1253, JCPDS International Center for Diffraction Data, Swarthmore, PA, USA.
8. K. Kim, G. Hanket, T. Huynh, and W. Shafarman, *J. Appl. Phys*. **111**, 83710 (2012).
9. S. Verma, TWF Russell, and R. Birkmire RW, *Proc. 23rd IEEE Photovoltaic Specialists Conference* 431 (1993).
10. K. Kim, E. Kimberly, A. Damiani, G. Hanket and W. Shafarman, *Proc. 38th IEEE Photovoltaic Specialists Conference* 1 (2012).
11. G. M. Hanket, R. Kamada, W. K. Kim, and W. N. Shafarman, *Proc. 33rd IEEE Photovoltaic Specialists Conference, (2008).*
12. R. Krishnan et al., *Progress in Photovoltaics* **20**, 54 (2012).
13. J. L. Shay and J. H. Wernick, Ternary chalcopyrite semiconductors: growth, electronic properties, and applications, Pergamon Press, New York, NY, **1975**.
14. Y. Tauchi, K. Kim, H. Park and W. Shafarman, *IEEE Journal of Photovoltaics*, **3**, 467-71 (2013).
15. AgIn, JCPDS card No. 25-0386, JCPDS International Centre for Diffraction Data, Swarthmore, Pennsylvania, USA.
16. M. Yuan, D. B. Mitzi, O. Gunawan, A. J. Kellock, S. J. Chey, and V. R. Deline, *Thin Solid Films,* **519**, 852 (2010).
17. T. Nakada, Y. Honishi, Y. Yatsushiro, and H. Nakakoba, Proc. *Proc 37th IEEE Photovoltaic Specialists Conference*, 3527 (2011).
18. B. M. Basol, V. K. Kapur, and R. J. Matson, *Proc. 22nd IEEE Photovoltaic Specialists Conference Photovoltaic Specialists Conference,* 1179 (1991).
19. K. Kim, J, Han and W. Shafarman, *Mat. Res. Soc. Symp. Proc.* **1538**, 15-20 (2013).
20. D. Abou-Ras et al., *Thin Solid Films* **480–481**, 433 (2005).
21. H. Simchi, B.E. McCandless, T. Meng, J.H. Boyle, and W.N. Shafarman, *Journal of Applied Physics*, **114**, 013503 (2013).
22. H. Simchi, B. McCandless, T. Meng, and W. Shafarman, *Journal of Applied Physics* **115**, 033514 (2014).

23. K. Kim, H. Park, G. Hanket, W.K. Kim and W. Shafarman, *Progress in Photovoltaics*, **23**, 765**–**772 (2015).
24. M. Bär, et al., Journal of Applied Physics **96**, 3857 (2004).
25. S-H. Wei and A. Zunger, *Journal of Applied Physics* **78**, 3846 (1995).
26. T. Maeda, T. Takeichi and T. Wada, *physica status solidi (a)* **203**, 2634 (2006).
27. S. Hegedus and W. Shafarman, *Progress in Photovoltaics* **12**,155-76 (2004).
28. S. Soltanmohammad, D. Berg, L. Chen, K. Kim, H. Simchi and W. Shafarman, *Proc. 40th IEEE Photovoltaic Specialists Conference*, 1707 (2014).
29. P.J. Wang, J.S. Kim, and C.C. Lee, J. Electron. Mater. **38**, 1860 (2009).
30. J.A. Venables, *Introduction to Surface and Thin Film Processes* (Cambridge University Press, 2000), p. 146.
31. V. Probst, J. Palm, S. Visbeck, T. Niesen, R. Tölle, a. Lerchenberger, M. Wendl, H. Vogt, H. Calwer, W. Stetter, and F. Karg, *Sol. Energy Mater. Sol. Cells* **90**, 3115 (2006).
32. D. Berg, C. Thompson and W. Shafarman, *Mat. Res. Soc. Symp. Proc.* **1538**, 3 (2013).
33. K. Kim, E, Eser and W. Shafarman, *IEEE Journal of Photovoltaics* **5** ,1222 (2015).